Combined targeting of glioblastoma stem cells of different cellular states disrupts malignant progression

🔴 Check for updates

A list of authors and their affiliations appears at the end of the paper

Glioblastoma (GBM) is the most lethal primary brain tumor with intra-tumoral hierarchy of glioblastoma stem cells (GSCs). The heterogeneity of GSCs within GBM inevitably leads to treatment resistance and tumor recurrence. Molecular mechanisms of different cellular state GSCs remain unclear. Here, we find that classical (CL) and mesenchymal (MES) GSCs are enriched in reactive immune region and high CL-MES signature informs poor prognosis in GBM. Through integrated analyses of GSCs RNA sequencing and single-cell RNA sequencing datasets, we identify specific GSCs targets, including MEOX2 for the CL GSCs and SRGN for the MES GSCs. MEOX2-NOTCH and SRGN-NFκB axes play important roles in promoting proliferation and maintaining stemness and subtype signatures of CL and MES GSCs, respectively. In the tumor micro-environment, MEOX2 and SRGN mediate the resistance of CL and MES GSCs to macrophage phagocytosis. Using genetic and pharmacologic approaches, we identify FDA-approved drugs targeting MEOX2 and SRGN. Combined CL and MES GSCs targeting demonstrates enhanced efficacy, both in vitro and in vivo. Our results highlighted a therapeutic strategy for the elimination of hetero-geneous GSCs populations through combinatorial targeting of MEOX2 and SRGN in GSCs.

Glioblastoma (GBM) is a primary malignant brain tumor of the central nervous system, with a high degree of malignancy and an annual inci-dence of 3–5 per 100,000 people[1]. Even with the most aggressive treat-ment strategies, the median survival is less than two years[2]. GBM is characterized by a high degree of intra- and inter-tumoral heterogeneity[3]. Studies over the last several decades have shown that GBM exhibits a wide range of cellular, genetic, epigenetic, and metabolic heterogeneity between tumors and even within individual tumors[4]. Single-cell RNA sequencing (scRNA-seq), spatial transcriptomics (stRNA-seq) and advanced computational analyses allow for comprehensive identification of cellular states affected by various tumor microenvironments. Analyses based on bulk expression profiles identified that three subtypes of GBM exist, namely proneural (PN), classical (CL), and mesenchymal (MES)[5,6]. Recent single-cell expression profiling studies found each GBM sample contains dynamic cellular states of tumor cells, and this intra-tumoral heterogeneity has potential prognostic implications[7–10].

GBM contain stem cell-like tumor-initiating cells named glio-blastoma stem cells (GSCs) that represent their driving force and exhibit preferential resistance to radiotherapy and chemotherapies[11–13]. GSCs are functionally distinct from differentiated tumor cells at multiple regulatory levels including unique epigenetic, transcriptional, and metabolic profiles[14–16]. Previous studies predominantly considered GSCs as a single-cell population to explore its functional mechanism. However, established GSCs markers are associated with distinct glio-blastoma cellular states. Among GSCs surface markers, CD24 is the highest in neural-progenitor-like (NPC-like) cells, CD133 in oligodendrocyte-progenitor-like (OPC-like) cells, EGFR in astrocyte-like (AC-like) cells, and CD44 in mesenchymal-like (MES-like) cells[17]. These results indicate that markers commonly used to define GSCs may identify distinct cellular states instead of a single, unified subpopula-tion. Previous studies have shown that heterogeneous GSCs reside in distinct niches, highlighting the need for tailored therapeutic

✉e-mail: yypl9@njmu.edu.cn; drjeremyrich@gmail.com; zhangwei_vincent@126.com; drxiuxingwang@163.com

approaches to target specific subsets within their respective microenvironments[18]. Although features of different cellular states of GSCs are distinct and subpopulations of GSCs might not be equally important for tumor progression, few studies have explored their molecular mechanisms. A comprehensive understanding of the biology of different cellular states of GSCs is needed for developing new GBM therapies.

In this work, we find that single GBM sample contains GSCs with different cellular states. CL and MES GSCs are predominantly found in immune-reactive regions, and a high CL-MES signature is associated with poor prognosis in GBM. MEOX2 and SRGN are identified as targets for CL and MES GSCs, respectively. The MEOX2-NOTCH and SRGN-NFκB axes drive proliferation while sustaining stemness and subtype features of CL and MES GSCs. Within the tumor microenvironment, these regulators confer resistance to macrophage mediated phagocytosis in CL and MES GSCs. Using genetic and pharmacologic approaches, we identify FDA-approved drugs targeting MEOX2 and SRGN. Combined CL and MES GSCs targeting demonstrates enhanced efficacy, both in vitro and in vivo. Targeted therapy tailored for CL and MES GSCs in their specific niches has the significant potential to improve the clinical outcome of GBM patients.

Results

Glioblastoma stem cells exhibit transcriptional heterogeneity and high CL-MES signature inform poor prognosis in glioblastoma

Studies of intratumoral subtype heterogeneity have proposed essential insights into the underlying biological mechanisms[5,6,8]. Analysis of the GSCs RNA-seq dataset (GSE119834) revealed that GSCs isolated from different GBM patients exhibit distinct transcriptional subtypes[5] (PN, CL, and MES) and cellular states[8] (NPC-like, OPC-like, AC-like, and MES-like) (Supplementary Fig. 1a and Supplementary Data 1). In previous reports, four tumor cellular states in each tumor defined by scRNA-seq are highly consistent with three bulk subtypes defined by TCGA. The TCGA-CL and TCGA-MES subtypes correspond to tumors enriched for the AC-like and MES-like states, respectively. The TCGA-PN subtype corresponds to the combination of the NPC-like and OPC-like states[8]. Our results also observed the same phenomenon. To examine GSCs composition within glioblastoma, we performed single-cell RNA sequencing from 24 samples (22 patients) dissociated and processed directly after surgical tumor resections. We interrogated six scRNA-seq datasets (GSE103224[19], GSE117891[20], GSE131928[8], GSE141383[21], GSE173278[22], and GSE182109[23]) of additional 58 IDH-wt GBM specimens for joint analysis to enhance the reliability of the screening results. After isolating tumor cells in scRNA-seq datasets, we defined GSC-like tumor cells as any cell expressing CD133, CD15 or OCT4, in conjunction with SOX2[24] (Supplementary Fig. 1b). Next, we classified GSC-like tumor cells into the four cellular states (NPC-like, OPC-like, AC-like, or MES-like) defined by Neftel et al.[8]. The proportion of four cellular states of GSC-like tumor cells were similar to the proportion of all tumor cells (Supplementary Fig. 1c). Most tumors containing all four cellular states of GSCs and the frequencies of GSC-like tumor cells states varied between tumors (Fig. 1a). These results revealed the heterogeneous GSCs populations, suggesting that no single therapeutic modality may be universally effective.

Subpopulations of GSCs might not all be equally important for GBM progression. GSCs are not uniformly distributed within tumors and critically interact with their microenvironment[18]. Interactions between GSCs and tumor immune microenvironment are closely related to GBM malignant progression[25,26]. In the Ivy Glioblastoma Atlas Project (Ivy GAP) database, which contains data from 42 GBM regionally microdissected with RNA-seq, samples in the immune response region showed higher CL and MES signatures (Supplementary Fig. 1d). Analysis of GSC-like tumor cells in the scRNA-seq dataset revealed that the spatially unique reactive-immune program[27] was

associated with AC- and MES-like states (Supplementary Fig. 1e). Co-labeling for CD45 and EGFR⁺SOX2⁺/CD44⁺SOX2⁺ region confirmed that CL and MES GSCs were enriched in reactive immune region in GBM (Supplementary Fig. 1f, g). These results imply potential interactions between CL and MES GSCs with tumor immune microenvironment.

To further investigate the clinical significance of intratumoral subtype heterogeneity characteristics, we analyzed the expression profiling data in clinical dataset. In our in-house generated clinical dataset, patients with high AC-like and MES-like GSCs proportion (>50%) had a shorter survival compared with patients with low proportion (<50%) (Fig. 1b and Supplementary Data 2). In TCGA GBM dataset, after obtaining the subtype signature scores of each GBM sample[5], we compared the association between the level of patient subtype score and survival prognosis. Patients with higher transcriptional signature scores for both CL and MES subtypes had a shorter survival, while higher scores for both PN and CL or higher scores for both PN and MES signatures did not show significance for the patient's survival (Supplementary Fig. 1h). These results indicate the vital roles of CL and MES GSCs in GBM malignant progression. Suggesting that combined CL and MES GSCs targeting may be effective in overcoming tumor malignant progression caused by intratumoral heterogeneity.

MEOX2 and SRGN are specific targets in classical and mesenchymal glioblastoma stem cells

To identify representative targets with clinical utility in CL and MES GSCs, we interrogated both single-cell and bulk RNA-seq datasets as illustrated in the flow chart shown in Fig. 1c. We selected genes that met the following conditions: First, genes that were highly expressed in classical signature (CL subtype and AC-like cellular state) or mesenchymal signature (MES subtype and MES-like cellular state) GSCs under the following conditions: (1) AC-like/MES-like GSC-like tumor cells vs. other cellular state GSC-like tumor cells (scRNA-seq datasets, n = 80); (2) CL/MES GSCs vs. CL/MES differentiated glioblastoma cells (DGCs) (in-house generated); (3) CL/MES GSCs vs. non-neoplastic neural stem cells (NSCs) (GSCs/NSCs dataset GSE119834); (4) CL/MES GSCs vs. other subtype GSCs (GSCs/NSCs dataset GSE119834)[28]; (5) GBM vs. non-neoplastic brain tissue (TCGA GBM HG-U133A); (6) CL/MES GBM vs. other subtype GBM (TCGA GBM HG-U133A). Second, expression of genes was positively correlated with CL/MES subtype signature score. Third, higher expression of genes was associated with poorer patient survival. After the above screening steps, MEOX2 and SRGN were selected as typical CL and MES GSCs targets for subsequent studies (Supplementary Data 3 and 4).

Survival analysis of the TCGA GBM dataset showed that patients with higher expression of MEOX2 and SRGN had worse survival prognoses than those with low expression of both genes (Fig. 1d). In scRNA-seq data, MEOX2 and SRGN are overexpressed in AC-like and MES-like tumor cells and GSC-like tumor cells, respectively (Fig. 1e and Supplementary Fig. 2a–h). In bulk RNA-seq data, MEOX2/SRGN were enriched in CL/MES GSCs and GBM, respectively. MEOX2 expression was positively correlated with the CL signature, whereas SRGN expression was correlated with the MES signature in GSCs (Fig. 1f and Supplementary Fig. 2i–l). Quantitative reverse transcription (RT)-PCR and immunoblot analysis confirmed the characteristic expression of MEOX2 and SRGN in CL and MES GSCs (Fig. 1g, h and Supplementary Fig. 3a, b).

To validate the reliability of screening results, we intensely interrogated the expression profiles of MEOX2 and SRGN in multi-omics data. H3K27ac is associated with transcriptional activation and is mainly enriched in enhancer and promoter regions[29]. Analysis of H3K27ac Chromatin Immunoprecipitation Sequencing (ChIP-seq) data of GSCs and NSCs[28] revealed that H3K27ac was enriched in the MEOX2 promoter regions of CL GSCs. In comparison, SRGN was marked explicitly by H3K27ac in MES GSCs (Supplementary Fig. 3c). Immunofluorescent staining showed a strong overlap between SOX2 and
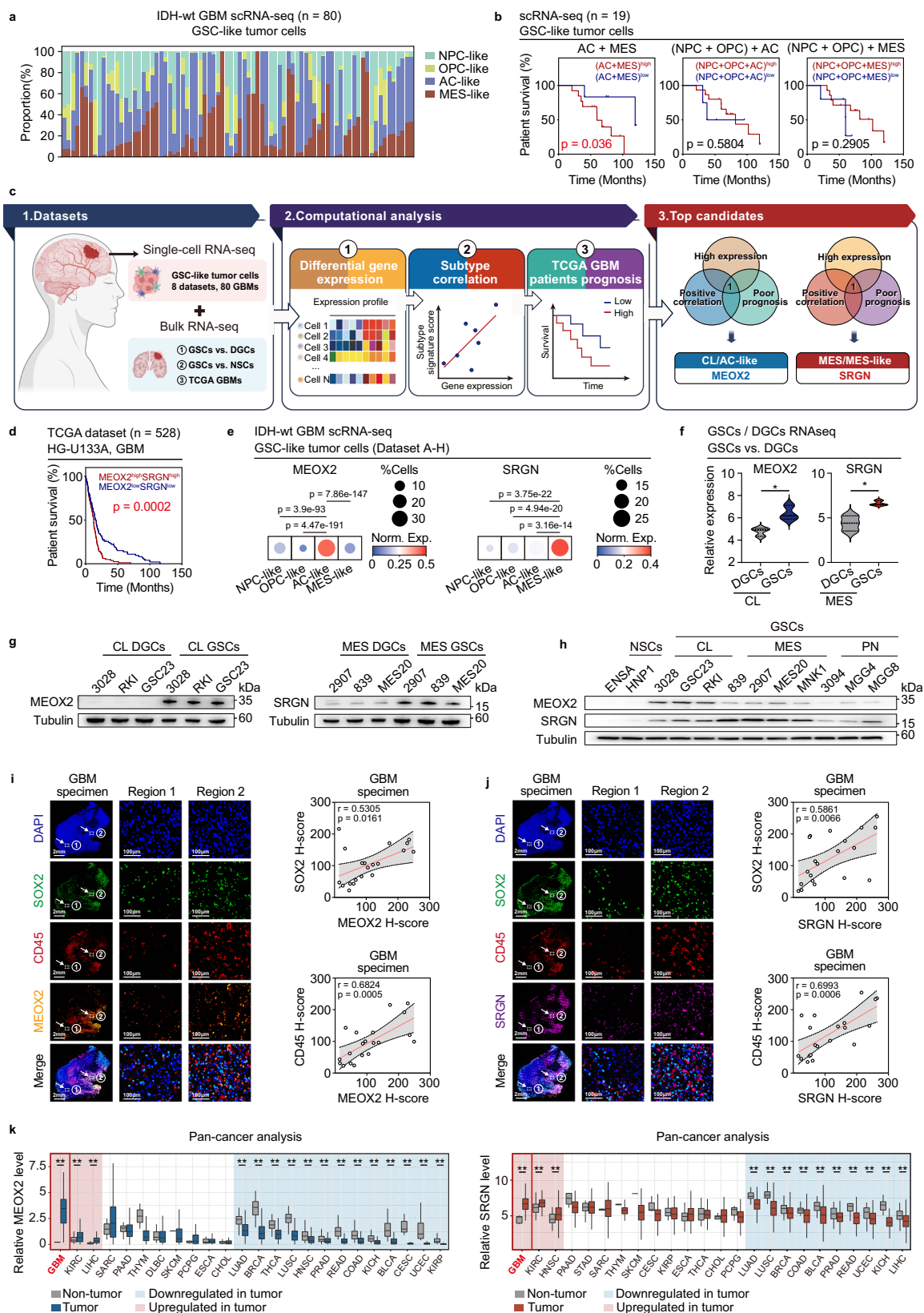
MEOX2/SRGN tumor cells in GBM surgical specimens, and co-labeling for CD45 and MEOX2/SRGN confirmed our analysis findings that CL and MES GSCs were enriched in reactive immune region in GBM (Fig. 1i, j and Supplementary Fig. 3d, e). By analyzing the GBM spatial transcriptomics data, we found that the spatial distribution of *MEOX2/SRGN* in GBM was consistent with the distribution of an

AC-like/MES-like signature. *MEOX2/SRGN* enriched regions overlapped with reactive immune regions (Supplementary Fig. 3f–h).

To evaluate the potential of MEOX2 and SRGN as therapeutic target, pan-cancer analysis was performed to examine their expression patterns across all tumor types. Interestingly, when comparing tumor vs. normal tissues expression across all cancer types, *MEOX2* and *SRGN*

Fig. 1 | MEOX2 and SRGN are enriched in CL and MES GSCs, respectively.
a Composition of four cellular states GSC-like tumor cells (SOX2⁺ in conjunction with CD133⁺/CD15⁺/OCT4⁺) in each GBM sample from scRNA-seq datasets. **b** Kaplan−Meier survival curves are shown for GBM patients in our in-housed generated scRNA-seq dataset, based on combination of GSC-like tumor cells proportion as indicated (high: >50%, low: <50%). **c** Diagram depicting the screening workflow to identify targets for CL/AC-like and MES/MES-like subtype GSCs. Created in BioRender. Wang, X. (2025) https://BioRender.com/f42j224.
d Kaplan−Meier survival curve of GBM patients from TCGA (HG-U133A) dataset, based on MEOX2 and SRGN expression (high: >50%, low: <50%). **e** Bubble plot showing proportions and normalized expression levels of MEOX2 and SRGN in different cellular state GSC-like tumor cells from scRNA-seq datasets. **f** MEOX2 (left) and SRGN (right) gene expression in the GSCs ($n = 3$)/DGCs ($n = 3$) RNA-seq dataset (in-house generated). *$p < 0.05$. **g** MEOX2 and SRGN protein levels were measured by western blotting in CL/MES DGCs ($n = 3$) and CL/MES GSCs ($n = 3$). Tubulin was

used as the loading control. **h** MEOX2 and SRGN protein levels were measured by western blotting in NSCs ($n = 2$) and GSCs ($n = 10$). Tubulin was used as the loading control. Immunofluorescence images showing co-staining of DAPI (blue), SOX2 (green), CD45 (red) with MEOX2 (yellow, **i**) or SRGN (purple, **j**) in glioblastoma samples. Scale bar, 2 mm (left), 100 μm (middle and right). The correlations between MEOX2/SRGN, SOX2, and CD45 expressions are shown. The gray area indicates the 95% CI of the regression. **k** Pan-cancer analysis of MEOX2 (left) and SRGN (right) expression levels in 24 different tumors from the TCGA dataset. **$p < 0.01$. Box plots show median (center line), 25th−75th percentiles (box bounds), and whiskers extend to minimum and maximum values within 1.5 times the interquartile range. Statistics: (**b**, **d**) Log-rank test. **e**, **f**, **k** Unpaired Student's t test for two-group comparison. **i**, **j** The Pearson correlation test. Images: **g**, **h** Representative blots ($n = 3$). **i**, **j** Representative images ($n = 30$). Source data are provided as a Source Data file.

exhibit the highest fold-change differences. When comparing expression levels across all tumor tissues, *MEOX2* ranked second, and *SRGN* ranked fifth in terms of expression among all cancer types (Fig. 1k). Previous studies have demonstrated important roles for MEOX2 and SRGN in other cancers, with MEOX2 functioning in lung cancer and SRGN in melanoma[30,31], However, their remarkably high differential expression in GBM, together with our findings of subtype-specific expression, suggests their particular promise as therapeutic targets in GBM.

MEOX2 and SRGN support cell proliferation, self-renewal, and stemness in a subtype-specific manner in classical and mesenchymal glioblastoma stem cells, respectively

To determine the functional importance of MEOX2 and SRGN in the corresponding GSCs, we depleted the expression of either MEOX2 or SRGN using two non-overlapping specific shRNAs in CL (3028 and RKI) and MES (2907 and 839) GSCs, respectively. MEOX2 depletion potently decreased the cell viability of CL GSCs, but with modest or no effects on MES and PN GSCs (Fig. 2a and Supplementary Fig. 4a, b). SRGN knockdown significantly reduced cell growth and proliferation of MES GSCs without affecting the expansion of CL and PN GSCs (Fig. 2b and Supplementary Fig. 4c, d). Stem cell frequency and self-renewal of GSCs were diminished upon MEOX2 or SRGN depletion, as revealed by GSCs neurosphere formation and extreme limiting dilution assays (Fig. 2c−f and Supplementary Fig. 4e, f). Conversely, overexpression of MEOX2 enhanced the proliferation of CL GSCs (Supplementary Fig. 4g−j). In MES GSCs, overexpression of SRGN promoted GSCs growth (Supplementary Fig. 4k−n). Reconstitution of MEOX2 expression in CL GSCs rescued the deficit of CL GSCs proliferation and self-renewal after MEOX2 knockdown (Supplementary Fig. 4o−r). Overexpression of SRGN rescued the proliferative and self-renewal capacity of MES GSCs carrying SRGN knockdown-mediated growth defects (Supplementary Fig. 4s−v).

RNA-seq analysis revealed that depletion of MEOX2 induced extensive gene expression changes in CL GSCs (Supplementary Fig. 5a, b). The deficiency of MEOX2 decreased the mRNA expression and protein levels of stem cell markers (SOX2 and ID1) in CL GSCs (Fig. 2g−i). After MEOX2 knockout, CL subtype marker genes expression significantly decreased, suggesting that MEOX2 was essential in maintaining CL status in CL GSCs (Supplementary Fig. 5c−e). In MES GSCs, the SRGN knockout group was transcriptionally distinct from the control group, with over 900 genes differentially expressed (Supplementary Fig. 5f, g). The deficiency of SRGN in MES GSCs decreased the expression of the stem cell markers (SOX2 and ID1) in MES GSCs (Fig. 2j−l). After SRGN knockout, the expression of many MES subtype marker genes significantly decreased (Supplementary Fig. 5h−j). These data indicate that MEOX2 and SRGN play important roles in maintaining the stemness and subtype signatures in CL and MES GSCs, respectively.

To investigate the in vivo function of MEOX2 and SRGN in tumor propagation in an orthotopic xenograft model, we implanted MEOX2-knockdown CL GSCs or SRGN-knockdown MES GSCs into the brains of immunocompromised mice. Bioluminescence imaging confirmed that the anti-tumor effects of MEOX2 knockdown in CL GSCs were more effective than in MES GSCs, whereas SRGN knockdown showed the opposite result. For mice bearing CL GSCs, MEOX2 knockdown prolonged the survival of intracranial tumor-bearing mice relative to the control group. In contrast, SRGN knockdown reduced the growth of MES GSCs-derived tumors (Fig. 2m−p). Collectively, these results showed that MEOX2 and SRGN play specific and vital roles in maintaining CL and MES GSCs, respectively.

MEOX2 mediates activation of the Notch signaling pathway in classical glioblastoma stem cells

MEOX2 belongs to the homeobox gene family of transcription factors[32,33]. 3028 was patient-derived xenograft models and were not sorted by subtype-specific surface markers. We performed single-cell RNA sequencing on 3028 GSCs. The analysis results showed that 3028 contained all four cellular states GSCs, among which AC-like had the highest proportion. After knocking out MEOX2 in 3028, we found a subtype transition in 3028 GSCs and the proportion of AC-like GSCs decreased (Fig. 3a, b and Supplementary Fig. 6a, b). To interrogate the mechanism of MEOX2 in maintaining CL GSCs, we performed multi-omics analysis including bulk RNA-seq and scRNA-seq after MEOX2 knockout and ChIP-seq for MEOX2 in CL GSCs (Fig. 3c).

For MEOX2 knockout RNA-seq data, we performed Gene set enrichment analysis (GSEA) using Hallmark, KEGG, and Reactome genesets. GSEA identified the enrichment of pathways associated with Notch signaling upon MEOX2 knockout, with many genes in the Notch signaling pathway being downregulated (Fig. 3d and Supplementary Fig. 6c). In scRNA-seq data, the enrichment level of Notch signaling decreased correspond with the decrease of AC-like proportion (Fig. 3e). Consistently, analysis of Hallmark, KEGG, and Reactome pathway genesets in GSCs RNA-seq and scRNA-seq datasets (GSC-like tumor cells) highlighted that Notch signaling was enriched in CL/AC-like GSCs, suggesting its key role in CL/AC-like GSCs (Supplementary Fig. 6d, e).

For MEOX2 ChIP-seq analysis, 17,153 distinct peaks were identified compared with the input control in total. MEOX2 tended to bind distally to coding regions, with many MEOX2 peaks in intergenic, intronic, and promoter regions (Supplementary Fig. 6f). To determine the biological functions of MEOX2 bound regions, we further investigated the genes proximal to MEOX2 binding sites. Consistent with previous findings, KEGG pathway enrichment analysis identified enrichment of the Notch signaling pathway (Fig. 3f). The recruitment of MEOX2 at the promoters of *JAG1*, *NOTCH1*, *MAML2*, *KAT2B*, and *PSEN1* was reduced upon loss of MEOX2, suggesting MEOX2 acted as a transcriptional activator of these genes. For *NOTCH2*, MEOX2 showed a distal binding
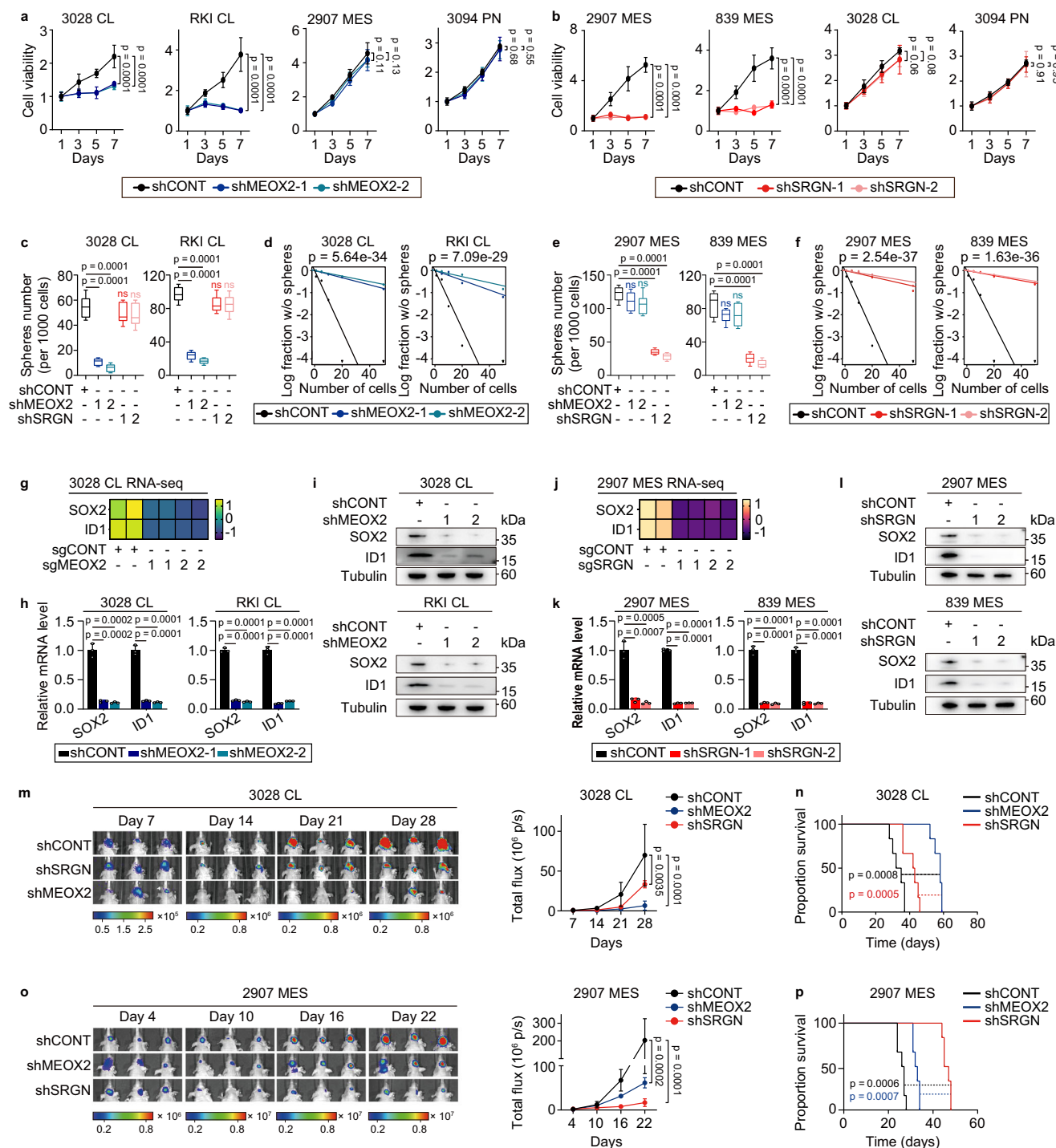
Fig. 2 | MEOX2 and SRGN are essential for GSCs proliferation, self-renewal, and stemness in CL and MES GSCs respectively. a, b Cell viability of indicated GSCs with shCONT, shMEOX2, or shSRGN measured by CellTiter-Glo assay ($n = 6$ per group). Data are presented as mean ± SD. **c, e** The number of spheres formed by CL and MES GSCs transduced with shCONT or shRNAs targeting MEOX2 or SRGN was quantified ($n = 6$ per group). Data are presented as mean ± SD. Box plots show median (center line), 25th–75th percentiles (box bounds), and whiskers extend to minimum and maximum values within 1.5 times the interquartile range. ns: non-significant. **d, f** In vitro limited dilution assay of CL and MES GSCs transduced with shCONT, shMEOX2-1/2 or shSRGN-1/2, respectively ($n = 30$ per group). χ2 test. **g, j** Heatmap of SOX2 and ID1 expression in MEOX2 and SRGN knockout RNA-seq data. **h, k** Quantitative RT-PCR assessment of SOX2 and ID1 mRNA levels in CL GSCs (3028, RKI) and MES GSCs (2907, 839) expressing shCONT, shMEOX2-1/2 or

shSRGN-1/2, respectively. Data are presented as mean ± SD. $n = 3$ per group. **i, l** IB analysis of SOX2 and ID1 levels in CL GSCs (3028, RKI) and MES GSCs (2907, 839) transduced with shMEOX2, shSRGN, or control shRNA, respectively.
m, o Bioluminescence imaging and quantification of orthotopic xenografts derived from luciferase-expressing 3028 (CL) and 2907 (2907) GSCs transduced with shCONT, shMEOX2, or shSRGN. Data are presented as mean ± SD. $n = 3$ per group. **n, p** Kaplan–Meier survival curves of mice bearing intracranial tumors derived from 3028 (CL) and 2907 (MES) GSCs ($n = 6$ per group) from the respective groups above. Statistics: **a, b, c, e, m, o** one-way ANOVA with Dunnett's multiple-comparison test. **d, f** χ² test for two-group comparison. **h, k** Unpaired Student's *t* test for two-group comparison. **n, p** Log-rank test. Images: **i, l** Representative blots ($n = 3$). Source data are provided as a Source Data file.
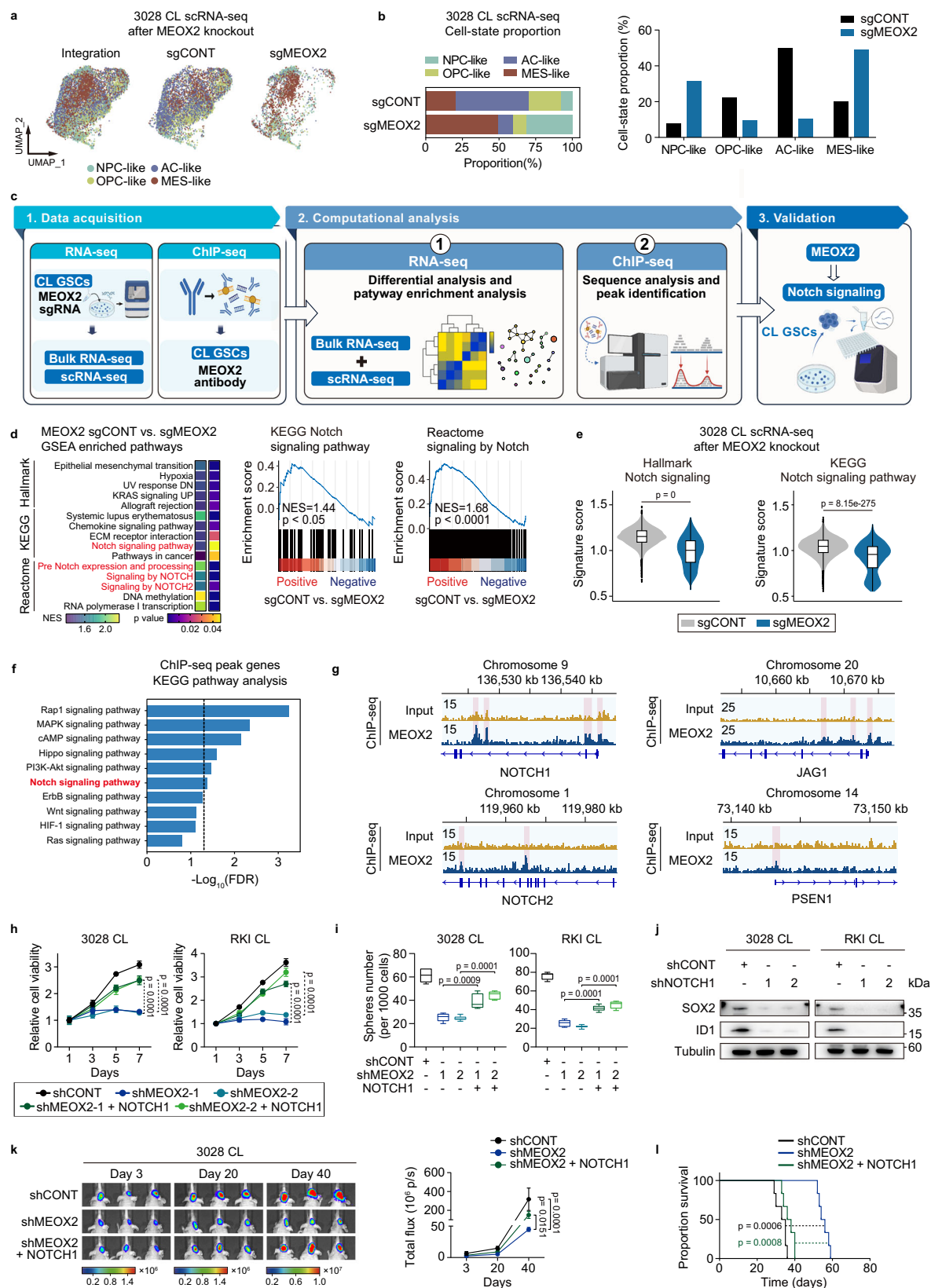
occupancy, with peaks located within intronic regions. This indicates that MEOX2 may bind to the enhancer regions at distal sites from the transcription start sites (Fig. 3g and Supplementary Fig. 6g). ChIP-qPCR analysis using the MEOX2 antibody revealed decreased enrichment at the promoter regions of *JAG1, NOTCH1, MAML2,* and *PSEN1* following MEOX2 knockdown (Supplementary Fig. 6h).

The inhibitory effect of MEOX2 knockdown on the expression of Notch signaling genes was validated by qRT-PCR in CL GSCs (Supplementary Fig. 7a). Overexpression of MEOX2 in MEOX2-depleted CL GSCs restored the expression levels of these genes (Supplementary Fig. 7b). Overexpressing NOTCH1 in CL GSCs with MEOX2 knockdown restored the defect in cell proliferation, suggesting that NOTCH

Fig. 3 | MEOX2 functions through transcriptional activation of the Notch signaling pathway in CL GSCs. a The UMAP plot of 3028 CL GSCs annotated by four cellular states. **b** Proportion changes of four cellular states cells in 3028 CL GSCs transduced with MEOX2 sgRNA or control sgRNA. **c** Diagram depicting the screening workflow to identify the MEOX2 downstream mechanism. Created in BioRender. Wang, X. (2025) https://BioRender.com/f42j224. **d** Gene set enrichment analysis (GSEA) of Hallmark, KEGG, and Reactome gene sets after MEOX2 knockout in 3028 (CL) GSCs. Normalized enrichment score (NES) and *p* values are shown by heatmap. **e** Violin-box plots showing the notch signaling score (Hallmark and KEGG) of the GSCs scRNA-seq data comparing sgCONT (*n* = 7078) vs. sgMEOX2 (*n* = 3168). Data are aggregated from technical replicates. **f** KEGG pathway enrichment analysis of MEOX2 ChIP-seq peak genes. **g** Input or MEOX2 binding signals of NOTCH1, NOTCH2, JAG1, and PSEN1 from Chip-seq on 3028 (CL) GSCs. **h** NOTCH1 overexpression rescued MEOX2 knockdown-induced cell viability decrease in CL GSCs (*n* = 6). Data are mean ± SD. **i** Sphere formation of CL GSCs with shCONT, shMEOX2, or shMEOX2 plus NOTCH1 overexpression (*n* = 6). Data are mean ± SD. **j** IB analysis of SOX2 and ID1 levels in 3028 (CL) and RKI (CL) GSCs transduced with NOTCH1 shRNA or control shRNA. **k** Bioluminescence images of mice with orthotopic xenografts from luciferase-expressing 3028 (CL) cells, showing tumor growth under shMEOX2 or shMEOX2 + NOTCH1 treatment (left). Luciferase signal intensities are shown (right). Data are mean ± SD; *n* = 3 biologically replicates per group. **l** Kaplan–Meier survival curves of mice bearing intracranial tumors derived from 3028 CL GSCs (*n* = 6) from the three groups in (**k**). Statistics: **d** The nominal p-value was calculated based on GSEA. **e** Unpaired Student's t-test for two-group comparison. **h, i, k** one-way ANOVA with Dunnett's multiple-comparison test. **l** Log-rank test. **e, i** Box plots show median (center line), 25th–75th percentiles (box bounds), and whiskers extend to minimum and maximum values within 1.5 times the interquartile range. Images: **j** Representative blots (*n* = 3). Source data are provided as a Source Data file.

signaling is a key downstream effector (Fig. 3h, i and Supplementary Fig. 7c). In CL GSCs, we knocked down NOTCH1 and found that the mRNA and protein levels of SOX2 and ID1 decreased (Fig. 3j and Supplementary Fig. 7d). Overexpression of NOTCH1 in CL GSCs restored the transcriptomic profile of the CL state in the MEOX2 knockdown GSCs (Supplementary Fig. 7e). Re-introducing NOTCH1 into CL GSCs with MEOX2 knockdown restored the in vivo growth of tumor (Fig. 3k, l). Overall, these results confirmed that MEOX2 mediates the activation of the Notch signaling pathway in CL GSCs. MEOX2-NOTCH axis plays an important role in CL GSCs' self-renewal and stemness maintenance.

SRGN protects NFKB1 from degradation to regulate NF-κB signaling in mesenchymal glioblastoma stem cells

The scRNA-seq results showed that 2907 contained all four cellular states GSCs, among which MES-like had the highest proportion. After knocking down SRGN in 2907, we found a subtype transition in 2907 GSCs and the proportion of MES-like GSCs decreased (Fig. 4a, b and Supplementary Fig. 8a, b). Given the critical role of SRGN in MES GSCs, we further explored its downstream mechanism. GSEA showed that the knockout of SRGN in MES GSCs reduced the expression of genes involved in nuclear factor-kappa B (NF-κB) signaling, tumor necrosis factor (TNF) signaling, and IL6-JAK-STAT3 signaling (Supplementary Fig. 8c). Analysis of Hallmark, KEGG, and Reactome pathway genesets in GSCs RNA-seq and scRNA-seq datasets (GSC-like tumor cells) revealed that these signals were characteristically enriched in MES/MES-like GSCs, indicating their important roles in MES/MES-like GSCs (Supplementary Fig. 8d, e). In scRNA-seq data, the enrichment level of NF-κB signaling decreased correspond with the decrease of MES-like proportion (Fig. 4c). We next analyzed the potential binding partners for SRGN using immunoprecipitation (IP) followed by mass spectrometry and found 670 proteins from the immunoprecipitants pulled down by SRGN (Supplementary Data 6). Gene Ontology (GO) terms in the biological process related to the NF-κB signaling and ubiquitin-proteasome system were enriched with these 670 candidate proteins (Fig. 4d and Supplementary Fig. 8f). Among them, NFKB1, a vital protein of the NF-κB signaling pathway, binds with SRGN (Supplementary Fig. 8g), suggesting that SRGN plays a crucial role in MES GSCs by modulating the NF-κB signaling pathway.

Further, we performed an IP assay and confirmed the mutual interaction between SRGN and NFKB1 in two MES GSCs (Fig. 4e). Immunofluorescence assays demonstrated that NFKB1 co-localized with SRGN in the cytoplasm of the MES GSCs (Fig. 4f). Gene expression analysis revealed that NFKB1 has a similar expression pattern as SRGN, which was also explicitly overexpressed in MES GSCs (Supplementary Fig. 8h). The same expression distribution of NFKB1 was also verified by scRNA-seq data (Supplementary Fig. 8i). However, SRGN knockdown did not alter NFKB1 mRNA levels (Supplementary Fig. 8j). In contrast, the depletion of endogenous SRGN led to a drastic decrease

in NFKB1 protein levels in two MES GSCs (Supplementary Fig. 8k), indicating that SRGN may regulate NFKB1 protein stability.

To determine the effect of SRGN on NFKB1 stability, we first blocked de novo protein synthesis using cycloheximide (CHX) and examined the NFKB1 and SRGN protein levels in MES GSCs. NFKB1 was gradually degraded within 8 h of CHX treatment in control cells (Supplementary Fig. 8l). Treatment of cells with the proteasome inhibitor MG-132 resulted in a significant increase in NFKB1 protein levels (Supplementary Fig. 8m). Blocking proteasomal degradation with MG-132 restored NFKB1 expression caused by SRGN knockdown (Supplementary Fig. 8n), but cycloheximide-chase analysis revealed that NFKB1 half-life was reduced by half in SRGN-depleted GSCs (Supplementary Fig. 8o). These results suggest that SRGN stabilizes the protein levels of NFKB1 in GSCs.

We identified that SRGN knockdown increased NFKB1 polyubiquitylation in MES GSCs (Fig. 4g). Next, we co-expressed Flag-NFKB1 and His-ubiquitin with HA-SRGN in MES GSCs. After the IP of NFKB1 from cells treated with MG132, we observed that NFBK1 was heavily ubiquitinated. However, co-expression of SRGN partially abolished NFKB1 ubiquitination (Fig. 4h). To examine the mechanistic basis of proteasomal degradation, we expressed NFKB1 with wild-type ubiquitin, K48-linked, or K63-linked polyubiquitylation. SRGN effectively disassembled the K48-linked polyubiquitylation of SRGN but had no significant effect on the nondegradative K63-linked polyubiquitylation of NFKB1 (Fig. 4i). Furthermore, we expressed a K48R form of ubiquitin in SRGN-depleted MES GSCs and found that K48R ubiquitin expression blocked NFKB1 downregulation induced by SRGN knockdown (Fig. 4j). These data confirmed that SRGN prevents polyubiquitylation and proteasome-mediated degradation of NFKB1.

NFKB1 downstream targets (*BIRC3, CXCL8, GADD45B, PLAU, TNFAIP3,* and *VCAM1*) were downregulated in SRGN knockout MES GSCs from RNA-seq data (Supplementary Fig. 9a). NFKB1 downstream targets also showed MES subtype characteristic expression patterns in the GSCs RNA-seq dataset (Supplementary Fig. 9b). qRT-PCR validated the effects of SRGN knockdown on decreasing mRNA expression of these targets in MES GSCs (Supplementary Fig. 9c). SRGN overexpression restored the decreased level of these target genes' expression in MES GSCs with SRGN knockdown (Supplementary Fig. 9d). Introducing NFKB1 into MES GSCs with SRGN knockdown restored the defect in cell proliferation and stem cell frequency (Fig. 4k, l and Supplementary Fig. 9e). Knockdown of NFKB1 decreased the mRNA and protein levels of SOX2 and ID1 in MES GSCs (Fig. 4m and Supplementary Fig. 9f). Overexpression of NFKB1 in MES GSCs restored the transcriptomic profile of the the MES state in the SRGN knockdown GSCs (Supplementary Fig. 9f). Re-introducing NFKB1 into MES GSCs with SRGN knockdown restore in vivo growth of tumor (Fig. 4n, o). These results confirmed that SRGN regulates the NF-κB signaling pathway by maintaining the protein stability of NFKB1. SRGN-NFκB axis plays significant roles in MES GSCs' self-renewal and stemness maintenance.
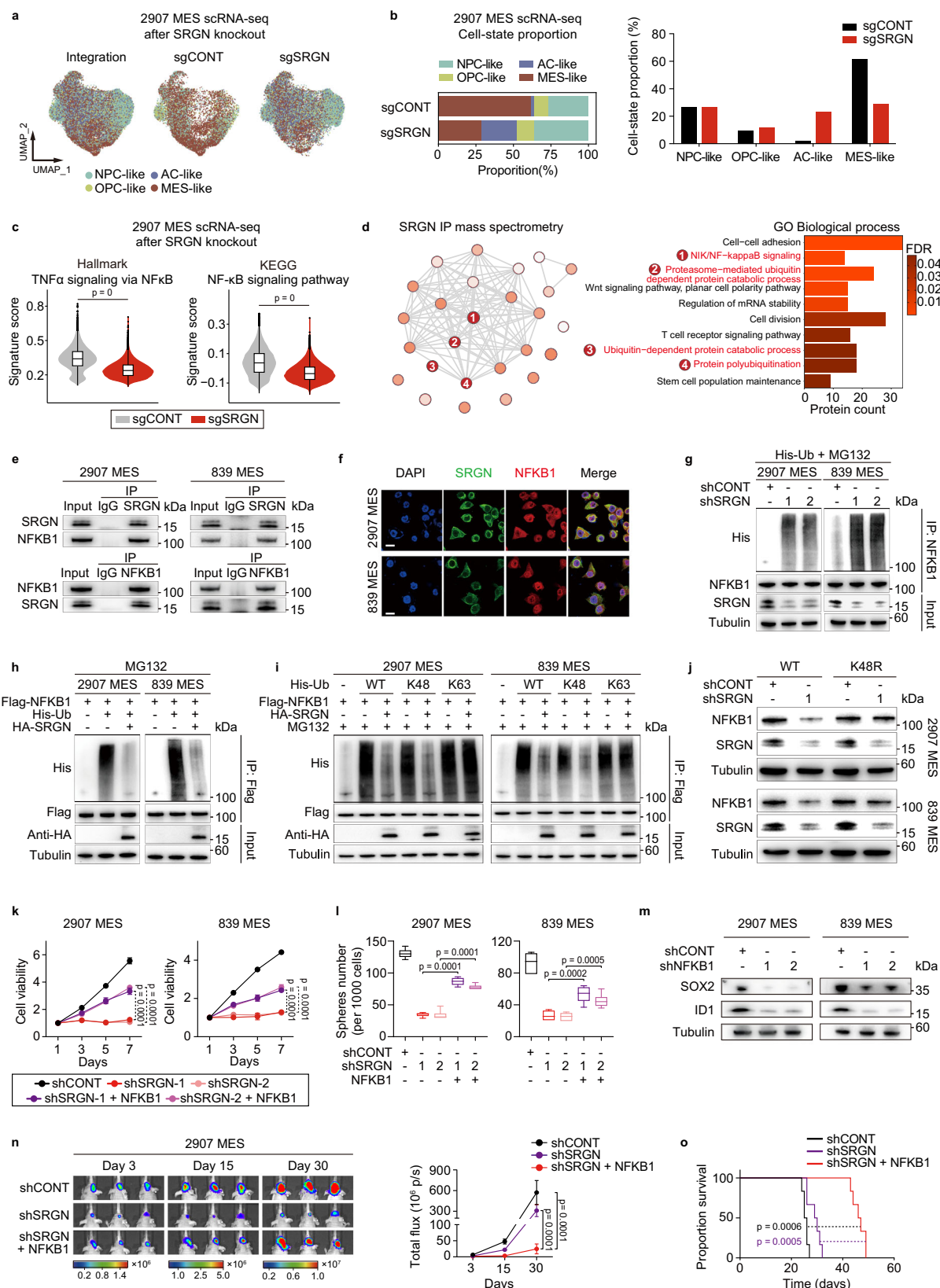
MEOX2 and SRGN regulate the resistance of classical and mesenchymal glioblastoma stem cells to macrophage phagocytosis, respectively

To explore the proportion of immune cells in different subtype GBM, we deconvoluted the TCGA GBM dataset by applying CIBERSORTx[34] using reference cell-state signatures derived from our in-house

generated single-cell transcriptomes (Supplementary Fig. 10a, b). We observed variations in cellular composition between different subtypes of GBM. The proportion of myeloid cells in GBM with high CL-MES signatures was significantly higher than that in GBM with low CL-MES signatures (Fig. 5a, b). To identify specific immune cells linked to CL-MES signature in GBM, we examined the TCGA GBM dataset for

Fig. 4 | SRGN promotes NF-κB signaling in MES GSCs post-transcriptionally by protecting NFKB1 from proteasomal degradation. a The UMAP plot of 2907 MES GSCs annotated by four cellular states. **b** Cellular states distribution in 2907 MES GSCs with SRGN or control sgRNA. **c** NF-κB signaling score (Hallmark and KEGG) of the GSCs scRNA-seq data comparing sgCONT ($n = 15{,}109$) vs. sgSRGN ($n = 24{,}993$). Data are aggregated from technical replicates. **d** GO analysis of 670 SRGN-interacting proteins identified by IP-MS. **e** MES GSCs lysates underwent SRGN/NFKB1 IP followed by IB, with IgG as control. **f** Representative images of SRGN and NFKB1 immunofluorescence in 2907 (MES) and 839 (MES) GSCs. Scale bar, 20 μm. **g** MES GSCs co-transfected with SRGN shRNA and His-Ub were treated with MG132 (20 μM, 8 h), followed by NFKB1 IP and His/SRGN IB. **h** MES GSCs co-transfected with SRGN shRNA and His-Ub were treated with MG132 (20 μM, 8 h), followed by NFKB1 IP and His/SRGN IB. **i** NFKB1 ubiquitylation assay in MES GSCs with indicated His-Ub constructs. **j** MES GSCs expressing Ub WT or Ub K48R were cultured with shCONT or shSRGN (72 h) and analyzed by NFKB1/SRGN IB. **k** NFKB1 over-expression rescued shSRGN-reduced viability in MES GSCs ($n = 6$). Data are presented as mean ± SD. **l** Cell counts of MES GSCs with shCONT, shSRGN, or shSRGN +NFKB1 ($n = 6$). Data are presented as mean ± SD. **m** IB analysis of SOX2 and ID1 levels in 2907 (MES) and 839 (MES) GSCs transduced with NFKB1 shRNA or control shRNA. **n** Bioluminescence images of MES GSCs xenografts with shSRGN or shSRGN +NFKB1 and quantification. Data shown as mean ± SD from 3 biological replicates. **o** Survival curves of mice with intracranial tumors from MES GSCs ($n = 6$ per group). Statistics: **c** Unpaired Student's t-test for two-group comparison. **k, l, n** one-way ANOVA with Dunnett's multiple-comparison test. **o** Log-rank test. **c, l** Box plots show median (center line), 25th–75th percentiles (box bounds), and whiskers extend to minimum and maximum values within 1.5 times the interquartile range. Images: **e, g–j, m** Representative blots ($n = 3$). **f** Representative images ($n = 3$). Source data are provided as a Source Data file.

immune cells using validated gene set signatures[35]. These analyses demonstrated that CL-MES signature correlated with significant enrichment of macrophages (Fig. 5c). The analysis of Rembrandt, CGGA, and Ivy GAP databases also obtained the same results (Supplementary Fig. 10c–k). These results indicated that CL and MES GSCs, which were enriched in the reactive immune region, may interact closely with macrophages in the tumor immune microenvironment.

Interactions between GSCs and the immune system represent a new and developing battleground with great implications for treatment. Further, we focused on the roles of MEOX2 and SRGN in the interaction between CL/MES GSCs and macrophages in the tumor microenvironment. In the scRNA-seq dataset, we found most anti-phagocytosis signals (MHC Class I genes, *CD24*, *PD-L1*, *CD47*, and *STC1*) were expressed significantly higher in AC-like and MES-like GSC-like tumor cells (Fig. 5d). In the GSCs RNA-seq dataset, we observed higher expression of most anti-phagocytosis signals in CL and MES GSCs compared with PN GSCs and NSCs (Fig. 5e). Knockout of MEOX2 decreased the expression level of anti-phagocytosis genes but with modest or no effects on the expression of macrophage chemokines and genes related to tumor-associated macrophage (TAM) polarization in CL GSCs (Fig. 5f and Supplementary Fig. 10l). In MES GSCs, SRGN knockout significantly decreased the expression of anti-phagocytosis genes (Fig. 5g). There were modest or no changes in the expression of macrophage chemokines and genes correlated with TAM polarization after SRGN knockout in MES GSCs (Supplementary Fig. 10m). These results were verified by qRT-PCR in CL and MES GSCs (Supplementary Fig. 10n, o). Under the co-culture system, MEOX2 depletion potently increased macrophage phagocytosis of CL GSCs, with modest effects on MES GSCs. Knockdown SRGN increased macrophage phagocytosis of MES GSCs, with modest effects on CL GSCs (Fig. 5h, i). These results indicated that MEOX2 and SRGN regulate the resistance of macrophage phagocytosis in CL and MES GSCs, respectively.
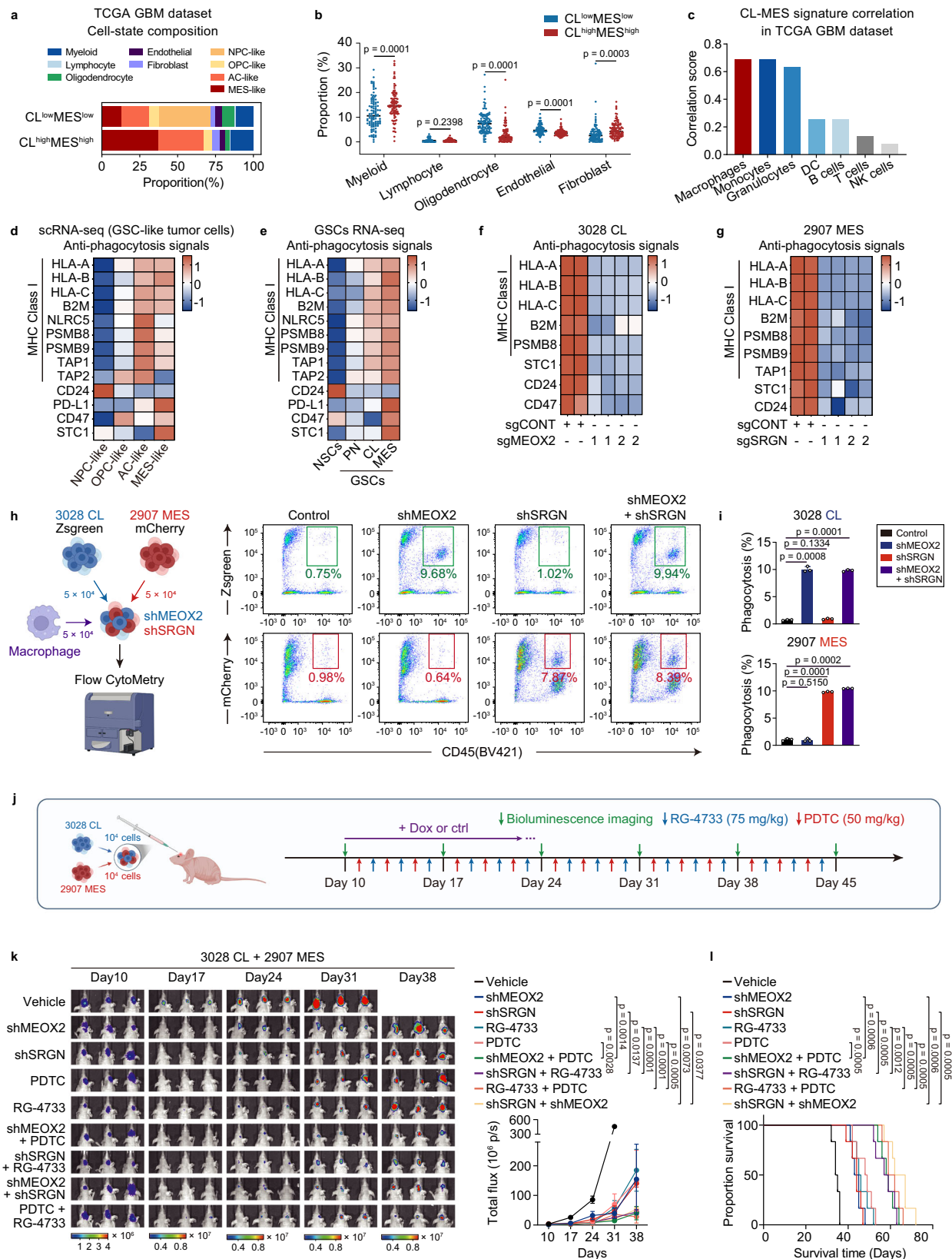
Combined targeting of classical and mesenchymal glioblastoma stem cells blocks tumor growth in a subtype-mixed glioblastoma model

Given that MEOX2-regulated genes are involved in the Notch signaling pathway. SRGN regulates the NF-κB signaling pathway by preventing NFKB1 from degradation. Given the absence of direct inhibitors targeting MEOX2 and SRGN, we focused on established pathway inhibitors to evaluate the therapeutic potential of dual targeting of CL and MES GSCs. Three widely used Notch inhibitors (DAPT, RG-4733, Semagacestat) and NF-κB inhibitors (BAY11-7082, JSH-23, PDTC) were prioritized for in vitro and in vivo validation. CL GSCs were generally more sensitive to Notch inhibitors, while MES GSCs displayed preferential sensitivity to NF-κB inhibitors. The half-maximal inhibitory concentration (IC_{50}) of NF-κB inhibitors was lower in MES GSCs than in CL GSCs. The differential sensitivity was confirmed by comparing the mean IC_{50} of Notch and NF-κB inhibitors in CL and MES GSCs, respectively (Supplementary Fig. 11a, b).

Systemic delivery of drugs against brain tumors requires sufficient drug delivery to the brain and the tumor site for maximal efficacy. Although GBM is often accompanied by disruption of the blood-brain barrier, this anatomic obstacle still portends a challenge to the effective drug delivery of many compounds. To identify the Notch and NF-κB inhibitors with sufficient brain penetration, we used high-performance liquid chromatography (HPLC) to detect inhibitor concentrations in the plasma and brain. RG-4733 and PDTC had better brain penetration than other compounds (Supplementary Fig. 11c, d). We determined an optimal concentration of each compound using synergy analyses to maximize the anti-tumor effect while limiting toxicities (Supplementary Fig. 11e). The differential sensitivity was confirmed by comparing the mean IC_{50} of Notch and NF-κB inhibitors in CL and MES GSCs (Supplementary Fig. 11f). The combination of low, clinically achievable concentrations of RG-4733 (Notch inhibitor) and PDTC (NF-κB inhibitor) blocked tumorsphere formation (Supplementary Fig. 11g). To explore the efficacy of combined targeting of CL and MES GSCs, we examined the therapeutic effects of RG-4733 and PDTC in a previously reported subtype-mixed model derived from a mixture of CL and MES GSCs (ratio 1:1)[18] (Fig. 5j). Orthotopic xenograft experiments subjected to a 9-arm experimental group including (1) vehicle control, (2) cells treated with shMEOX2, (3) cells treated with shSRGN, (4) in vivo treatment with the Notch inhibitor PDTC, (5) in vivo treatment with the NF-κB inhibitor RG-4733, (6) shMEOX2 plus PTDC, (7) shSRGN plus RG-4733, (8) shMEOX2 plus shSRGN, and (9) PDTC plus RG-4733. Bioluminescence imaging confirmed that the antitumor effects of combined therapy were more effective than monotherapy in both shRNA and small molecular inhibitor groups (Fig. 5k), with significantly prolonged survival with combined treatment (Fig. 5l), indicating that the combinatorial inhibition was an effective strategy for the heterogeneous cellular composition of GSCs.

Combined pharmacological inhibition of MEOX2 and SRGN with FDA-approved drugs is an effective treatment strategy

MEOX2 and SRGN have great potential to be therapeutic targets. We then developed a pipeline to identify compounds with likely inhibitory effects and favorable pharmacokinetic parameters (Fig. 6a). We started with a panel of FDA-approved drugs with known blood-brain barrier penetrance to perform virtual molecular screening. The DNA binding region of MEOX2 (residues 187-246) and the binding pocket of SRGN (residues 28-60) were predicted by the Alphafold 2 database model[36]. The drug's binding score was ranked according to the value of Gibbs free energy (Supplementary Data 7). We identified the top 30 drugs that might target MEOX2 or SRGN and verified them individually according to the high to low scores (Fig. 6b and Supplementary Fig. 12a, b). Targeted inhibition of these drugs on MEOX2 and SRGN was confirmed through a series of in vitro experiments. First, as mentioned previously, the CL and MES GSCs showed different reactivity to MEOX2 and SRGN inhibition. We tested the anti-tumoral efficacy of candidate drugs in CL and MES GSCs. Second, to further verify

a TCGA GBM dataset Cell-state composition

b

c CL-MES signature correlation in TCGA GBM dataset

d scRNA-seq (GSC-like tumor cells) Anti-phagocytosis signals

e GSCs RNA-seq Anti-phagocytosis signals

f 3028 CL Anti-phagocytosis signals

g 2907 MES Anti-phagocytosis signals

h

i 3028 CL

2907 MES

j

k 3028 CL + 2907 MES

l

the targeted inhibition effect of these drugs on MEOX2 and SRGN, we detected the changes in downstream targets of MEOX2 and SRGN after drug treatment. Third, we confirmed the binding of these drugs to MEOX2 and SRGN proteins through an affinity experiment. We used bio-layer interferometry (BLI) to detect the binding of candidate drugs with MEOX2 or SRGN.

Among the top 30 MEOX2-targeting candidates, nilotinib and dihydroergocristine (DHEC) were the most effective drugs against CL GSCs. Among the top 30 SRGN-targeting candidates, MES GSCs displayed preferential sensitivity to paliperidone and risperidone (Fig. 6c and Supplementary Fig. 12c, g). After treatment with nilotinib or DHEC, the expression of MEOX2 downstream targets was significantly

Fig. 5 | MEOX2 and SRGN regulate the resistance of CL and MES GSCs to macrophage phagocytosis, respectively. a Stacked bar plots indicate the cell composition of CL[low]MES[low] ($n = 109$) and CL[high]MES[high] ($n = 109$) GBM in the TCGA GBM dataset based on the single-cell-based deconvolution method, CIBERSORTx. **b** Comparison of the proportion of cell composition between CL[low]MES[low] ($n = 109$) and CL[high]MES[high] ($n = 109$) GBM in the TCGA GBM dataset. **c** Correlation coefficient between CL-MES signatures and various types of immune cell signatures in TCGA GBM dataset ($n = 528$). **d** Heatmap of anti-phagocytosis genes expression between four cellular state[8] GSC-like tumor cells in scRNAseq datasets. **e** Heatmap of anti-phagocytosis genes expression between three subtypes[5] GSCs in GSCs RNA-seq datasets (GSE119834). **f** Heatmap of anti-phagocytosis genes expression in MEOX2 knockout RNA-seq data. **g** Heatmap of anti-phagocytosis genes expression in SRGN knockout RNA-seq data. **h** Representative flow cytometry plots depicting the phagocytosis of GSCs transduced with shCONT, shMEOX2, shSRGN, or shMEOX2 + shSRGN co-cultured with macrophages. Created in BioRender. Wang, X. (2025) https://BioRender.com/f42j224. **i** Flow cytometry quantifies phagocytosis of

CL + MES GSCs treated with shMEOX2, shSRGN, or dual treatment versus control. Data are presented as mean ± SD. $n = 3$ per group. **j** Experimental design to assess in vivo effects of combinatorial targeting of CL and MES on xenograft of mixed CL (3028) and MES (2907) GSCs. Created in BioRender. Wang, X. (2025) https://BioRender.com/f42j224. **k** Bioluminescence images show the effect of combined treatment with 75 mg/kg RG-4733 and 50 mg/kg PDTC every two days on tumor growth in mice bearing mixed CL and MES xenografts derived from luciferase-expressing 3028 (CL) and 2907 (MES) GSCs. Time points indicate days post-intracranial injection (left), with luciferase signal intensities shown (right). Data are presented as mean ± SD. $n = 3$ biologically independent mice per group. **l**, Kaplan–Meier survival curves for mice bearing subtype-mixed orthotopic tumors (3028 CL and 2907 MES) ($n = 6$) after combined treatment of 75 mg/kg RG-4733 every two days and 50 mg/kg PDTC every two days. Statistics: **b, i** Unpaired Student's t test for two-group comparison. **k** one-way ANOVA with Dunnett's multiple-comparison test. **l** Log-rank test. Source data are provided as a Source Data file.

decreased in CL GSCs (Fig. 6d and Supplementary Fig. 13a). The downstream targets of SRGN were substantially reduced after treatment with paliperidone or risperidone in MES GSCs (Supplementary Fig. 13b, c). Protein levels of NFKB1 decreased after treatment with paliperidone or risperidone in MES GSCs (Fig. 6e and Supplementary Fig. 13d). The effects of these drugs on these downstream targets have been documented in several studies. Specifically, nilotinib was shown to decrease NOTCH1 expression in hepatocellular carcinoma (HCC) cell lines[37]. DHEC is a part of the ergoloid mixture products that directly inhibit γ-secretase[38]. Additionally, risperidone and paliperidone were demonstrated to exert their anti-inflammatory effects through inhibition of the NF-κB signaling pathway[39,40]. In CL and MES GSCs, the mRNA and protein levels of SOX2 and ID1 decreased after nilotinib/DHEC and paliperidone/risperidone treatment, respectively (Supplementary Fig. 13e–h). Nilotinib and DHEC treatment increased macrophage phagocytosis of CL GSCs. Paliperidone and risperidone treatment increased macrophage phagocytosis of MES GSCs (Supplementary Fig. 13i–l). Finally, based on K_d values, these four drugs were inferred to interact directly with MEOX2 or SRGN and the binding of drugs to truncated proteins was weak (Fig. 6f–j). To determine the combinatorial efficacy, we interrogated the effects of a range of concentrations of each drug against two CL and MES GSCs. Synergy analysis of four drugs showed that the combination of nilotinib and paliperidone had the best synergetic effect (Supplementary Fig. 14d–g).

GSCs WL1 were derived in our laboratory from a 55-year-old male patient with recurrent GBM. We performed scRNA-seq on WL1 to determine its cellular states distribution. The results showed that WL1 contained cells of all four cellular states. The proportions of four cellular states cells in WL1 were as follows: NPC-like (33.44%), OPC-like (13.17%), AC-like (14.83%), MES-like (38.56%) (Fig. 7a). GSCs WL1 were functionally validated by in vivo serial transplantation assays (Fig. 7b–h). To isolate cells of CL/AC-like and MES/MES-like features, we isolated EGFR-high (CL/AC-like cell-surface marker) and CD44-high (MES/MES-like cell-surface marker) cells from WL1. Both qPCR and Western blot results showed that MEOX2 was enriched in EGFR + WL1 GSCs (representing AC-like cellular states), while SRGN displayed high expression in CD44 + WL1 GSCs (representing MES-like cellular states) (Supplementary Fig. 14a–c). We then implanted these GSCs (1:1) orthotopically into immunocompromised mice to establish the model (Fig. 7i). Next, we examined the therapeutic effects of drugs on this model. Bioluminescence imaging confirmed that combined therapy was more effective than monotherapy or vehicle control. These in vivo results translated into superior survival with combined treatment (Fig. 7j–m). The therapeutic effects of drugs on mice bearing intracranial tumors derived from a mixture of CL and MES GSCs showed the same results (Supplementary Fig. 14h–l). These results indicated that combined targeting of CL and MES GSCs with FDA-approved agents is an effective treatment strategy for heterogeneous GBM. Taken

together, our study identified key drivers and downstream signaling pathways that govern CL and MES GSCs states. We provided clinically actionable drug candidates that serve as an avenue for combination therapies against a lethal and heterogeneous cancer (Supplementary Fig. 15).

Discussion

High intratumoral heterogeneity is one of the hallmarks of GBM[3]. From the therapeutic perspective, this heterogeneity is a major clinical obstacle in designing effective treatment strategies for GBM patients. Clinically relevant GBM subtypes have been defined based on the presence of IDH1/2 gene mutations[41]. Bulk and single-cell transcriptional profiling identified dynamic cellular states influenced by underlying somatic alterations and interactions with the tumor microenvironment[42–45]. Reversibly transition of tumor cells could occur between different cellular states in response to genetic, micro-environmental and therapeutic stimuli[46–48]. This cellular plasticity complicates the study of GBM heterogeneity.

GSCs are thought to contribute to intertumoral and intratumoral heterogeneity, although the extent of their role and the mechanisms involved remain areas of investigation. Single-cell sequencing and lineage tracking methods confirmed the existence of stem-like cancer cells in GBM, supported their importance in maintaining cell hierarchy, and further strengthened the concept of cell plasticity[49,50]. Although various markers can be enriched for GSCs, the distinct molecular mechanisms of GSCs in these cancer subtypes have not been explored thoroughly. In this study, we found that high CL and MES GSCs proportion within tumors was associated with poor prognosis of GBM patients. Through integrative analysis of gene expression programs underlying GSCs, we surveyed scRNA-seq and bulk RNA-seq datasets. MEOX2 and SRGN were identified as characteristic targets of CL and MES GSCs, respectively, with targeted therapeutic utility.

MEOX2 belongs to the homeobox genes family of transcription factors[32,33]. These transcription factors can promote cell growth, migration, angiogenesis, and maintain cell quiescence[51]. Recent studies have revealed that MEOX2 acts as a critical transcriptonal regulator in GBM progression. MEOX2 promotes GBM progression by driving epithelial-mesenchymal transition, cytoskeletal dynamics, and focal adhesion formation, thereby enhancing tumor cell invasion and proliferation, both of which are critical for tumor cells survival and growth[52,53]. Our data extends these findings by showing that MEOX2 is enriched in CL GSCs. MEOX2-NOTCH axis plays an important role in CL GSCs' self-renewal and stemness maintenance. SRGN is a low molecular weight glycoprotein distributed in the cytoplasm. SRGN plays an essential role in the storage and secretion of cytokines, chemokines, and proteases and has been reported to participate in many physiological and pathological processes[54]. Recent studies highlighted SRGN's importane in GBM biology. SRGN facilitates glioblastoma
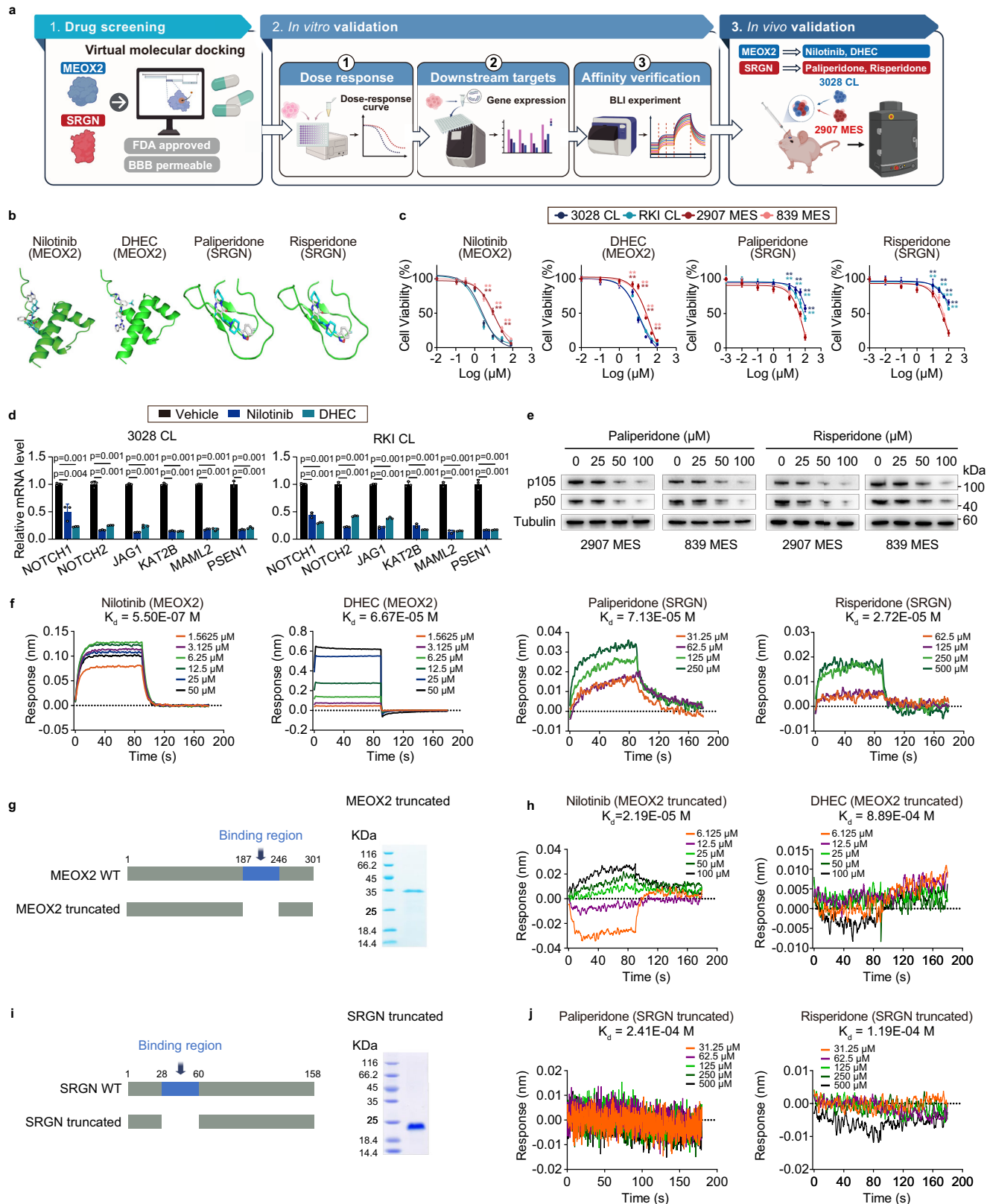
invasion, metastasis, and immune evasion by enhancing inflammatory and proteolytic signaling cascades[55,56]. Our results demonstrated that SRGN was a representative target of MES GSCs. SRGN characteristically regulated the proliferation and stemness of MES GSCs. SRGN regulated the NF-κB signaling pathway by maintaining NFKB1 protein stability.

Prior studies have highlighted the heterogeneous distribution of GSCs across distinct niches, necessitating subtype-specific therapeutic

strategies tailored to their microenvironment context[18]. While cellular heterogeneity exists among GSCs states, their contributions to tumor progression are not equivalent. Our analysis revealed that both CL and MES GSCs concentrate in regions with high immune cell presence, particularly marked by macrophage infiltration. As key innate immune sentinels, macrophages exhibit dual regulator roles mediated by competing pro-phagocytic ligands and immunosuppressive

Fig. 6 | Nilotinib and DHEC have inhibitory effects on MEOX2, while paliperidone and risperidone have inhibitory effects on SRGN. a Workflow of experimental strategy for finding MEOX2 and SRGN targeting drugs. Created in BioRender. Wang, X. (2025) https://BioRender.com/f42j224. **b** MEOX2 (residues 187-246) was docked with nilotinib and DHEC, and SRGN (residues 28-60) was docked with paliperidone and risperidone. **c** Dose-response curves for nilotinib, DHEC, paliperidone, and risperidone in CL GSCs (3028 and RKI) and MES GSCs (2907 and 839). Data are presented as mean ± SD. $n = 6$ biologically independent replicates per group. **$p < 0.01$. **d** Effects of nilotinib and DHEC on Notch signaling pathway genes (NOTCH1, NOTCH2, JAG1, KAT2B, MAML2, and PSEN1) expression in 3028 (CL) and RKI (CL) GSCs. Data are presented as mean ± SD from three independent experiments. **e** IB analysis of NFKB1 expression in 2907 (MES) and 839 (MES) GSCs treated with paliperidone or risperidone. **f** Bio-layer interferometry (BLI) was used to detect the equilibrium dissociation constant (K_d) between nilotinib with MEOX2, DHEC with MEOX2, paliperidone with SRGN, and risperidone with SRGN. **g** (Left) Schematic representation of MEOX2 truncated protein. (Right) Coomassie blue-stained SDS-PAGE gel of truncated MEOX2 protein. **h** Bio-layer interferometry (BLI) was used to detect the equilibrium dissociation constant (K_d) between nilotinib and DHEC with truncated MEOX2 protein. **i** (Left) Schematic representation of SRGN WT and truncated mutants with binding region indicated (amino acids 28-60). (Right) Representative Coomassie blue-stained SDS-PAGE gel showing purified truncated SRGN protein. **j** Bio-layer interferometry (BLI) was used to detect the equilibrium dissociation constant (K_d) between paliperidone and risperidone with truncated SRGN protein. Statistics: **c**, **d** Unpaired Student's t test for two-group comparison. Images: **e** Representative blots ($n = 3$). **g**, **i** Representative images ($n = 3$). Source data are provided as a Source Data file.

checkpoint molecules that modulate tumor cell clearance[57]. Dominant engagement of inhibitory receptors in these niches suppresses macrophage phagocytic activation, creating immune-evasive microdomains. The best-studied inhibitory receptor on macrophages is SIRPα, which recognizes as ligand the cell surface molecule CD47, often overexpressed on tumor cells[58]. Reprogramming tumor-promoting macrophages into tumor-suppressive macrophages can effectively inhibit GBM growth[59]. It was shown that inhibition of the CD47-SIRPα (signal regulatory protein α) axis in TAMs inhibited brain tumor growth in animal models[60,61]. Therefore, the methods related to enhancing the phagocytic effect of macrophages on GSCs also have high research significance. We found high expression of anti-phagocytosis checkpoint in CL and MES GSCs. MEOX2 and SRGN are involved in regulating anti-phagocytosis checkpoint expression in CL and MES GSCs, respectively. Targeting MEOX2 and SRGN enhanced macrophage phagocytosis of CL and MES GSCs.

Due to the limited benefit of a single targeted drug in improving patient survival, studying treatment strategies that combine different targeted drugs is becoming a viable strategy. Combining drugs could overcome some of the problems associated with GBM treatment. For example, a phase II clinical trial combined using bevacizumab and the topoisomerase inhibitor irinotecan prolonged median overall survival times to 9.2 months compared to 8.7 months with bevacizumab alone in recurrent GBM[62]. Although some research progress has been made using traditional methods such as combined radiotherapy and chemotherapy, there is still much room for improvement given the improved understanding of the molecular underpinning of GBM. MEOX2 and SRGN are targets representing CL and MES subtype properties in GSCs, respectively. Using virtual molecular screening combined with experimental validation, we identified drugs that target MEOX2 and SRGN. These FDA-approved drugs can cross the blood-brain barrier. For drug targeting MEOX2, nilotinib is a tyrosine kinase inhibitor used for the chronic phase treatment of chronic myeloid leukemia (CML). For drug targeting SRGN, paliperidone is a second-generation antipsychotic (SGA) medication used to treat several mental health conditions, including schizophrenia and bipolar disorder. We first reported the efficacy of targeting MEOX2 with nilotinib and SRGN with paliperidone. Our findings further extend the indications for these agents and provide a rationale for conducting clinical trials combining targeted CL and MES GSCs.

The proportion of GSCs in each cellular state varies among patients. Each cellular state defines the types of stress response it can mount, which may affect the clinical response of targeted therapy[63]. Directing therapeutics against the cellular form will be a priori addressed for each resistant mechanism mediated by that state. Our study offers a practical therapeutic strategy to co-opt state selective lethality in a preclinical model. Our investigation discovered that the representative targets MEOX2 and SRGN in CL and MES GSCs. We provided a deep understanding of the distinct regulatory mechanisms of CL and MES GSCs. Our data demonstrated the efficacy of rationally designed combinatorial targeting approaches. Using genetic and pharmacologic techniques, we found that combination therapy with FDA-approved agents targeting both CL and MES GSCs resulted in a significant reduction in tumor growth in our experimental models. Combinatorial targeting based on the improved understanding of intratumoral heterogeneity at the single-cell level will inform future clinical trial design in GBM.

Methods
Ethics statement
The study was conducted in accordance with the declaration of Helsinki and approved by Ethics Committee of the First Affiliated Hospital of Nanjing Medical University (2021-SR-076), Beijing Tiantan Hospital, Capital Medical University (KYSQ2019-200-01), and Case Western Reserve University (090401). We have obtained informed consent from all participants for publishing their individual-level data as presented in Supplementary Data 2 and 5.

Human glioblastoma samples
The scRNA-seq dataset 1 were derived from 7 samples. The 7 GBM specimens were obtained from the Department of Neurosurgery, The First Affiliated Hospital of Nanjing Medical University. Written informed consent was obtained from all patients. All patient studies were conducted in accordance with the recognized ethical guidelines of the Declaration of Helsinki and Ethics Committee of the First Affiliated Hospital of Nanjing Medical University (2021-SR-076).

For GBM specimens in scRNA-seq dataset 2, 15 patients (17 samples) with GBM were enrolled and pathologically diagnosed with GBM at Beijing Tiantan Hospital, Capital Medical University. All patients provided written informed consent for sample collection and data analyses. The Research and Ethical Committee approved this study of Beijing Tiantan Hospital, Capital Medical University (KYSQ2019-200-01). Fresh tumor samples were surgical resected from the above patients.

The available clinical characteristics of these patients are summarized in Supplementary Data 2. Sex and gender information was collected for all participants. However, sex and gender were not included as variables in the primary analysis. This study focused on characterizing the molecular mechanisms specific to distinct GSCs subtypes within individual GBM patients, where these intrinsic cellular properties and regulatory mechanisms have not been shown to be significantly influenced by sex and gender in previous studies[5,8].

Patient-derived and cell-line models
Glioblastoma tissues of GSCs were obtained from excess surgical resection samples from patients who underwent treatment at Case Western Reserve University and the First Affiliated Hospital of Nanjing Medical University after review by neuropathology with appropriate consent and in accordance with an Institutional Review Board-approved protocol (090401 and 2021-SR-076). All samples were examined by neuropathologists. Patient-derived xenografts were propagated as a renewable source of GSCs, to minimize in vitro artifacts from cell culture. All GSCs were derived as reported
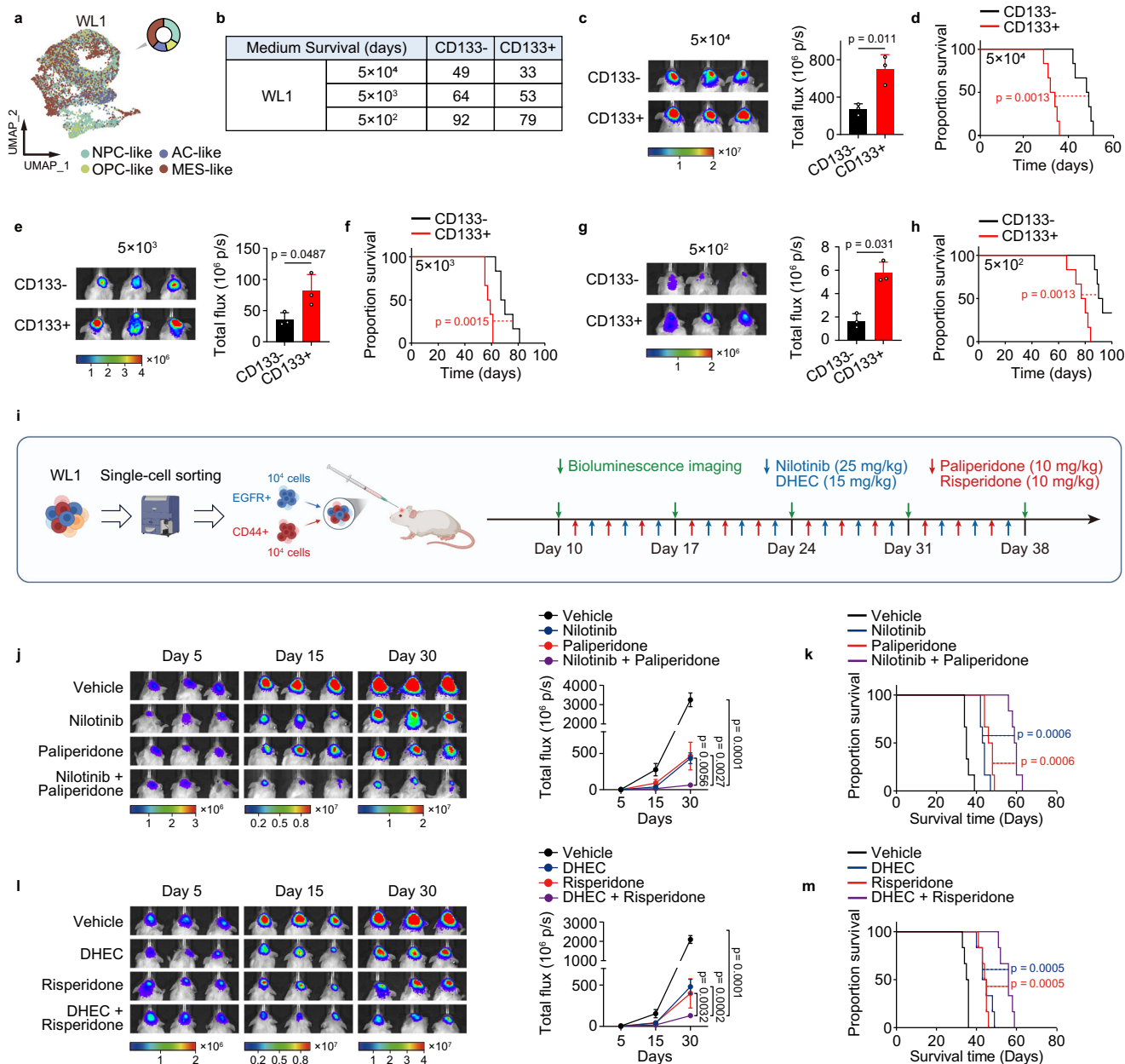
Fig. 7 | In vivo therapeutic efficacy of combined pharmacological inhibition of MEOX2 and SRGN in a subtype-mixed glioblastoma model. a Four tumor cellular states mapped in UMAP coordinates from WL1 scRNA-seq data. **b** Summary of mice medium survival in the in vivo limiting dilution assay. **c**, **e**, **g** Bioluminescence images of mice bearing xenografts derived from luciferase-expressing WL1 GSCs with the indicated numbers of cells are shown (left). In vivo bioluminescence imaging and intensities of luciferase signal in mice are shown (right). Data are presented as mean ± SD. $n = 3$ biologically independent mice per group. **d**, **f**, **h** Kaplan−Meier survival curves of mice implanted with the indicated numbers of WL1 GSCs ($n = 6$) are shown. **i** Experimental design to assess in vivo effects of nilotinib/DHEC and paliperidone/risperidone on xenograft of mixed CL (EGFR⁺) and MES (CD44⁺) WL1 GSCs. Created in BioRender. Wang, X. (2025) https://

BioRender.com/f42j224. **j**, **l** Bioluminescence images of mice bearing mixed CL and MES xenografts derived from luciferase-expressing WL1 GSCs, showing the effect of combined treatments (nilotinib + paliperidone or DHEC + risperidone) on tumor growth. Time points indicate days after intracranial injection of mixed GSC populations (left). Intensities of luciferase signal in mice are shown (right). Data are presented as mean ± SD. $n = 3$ biologically independent mice per group. **k**, **m** Kaplan−Meier survival curves for mice bearing subtype-mixed orthotopic tumors (WL1) after combined treatments of nilotinib (25 mg/kg) + paliperidone (10 mg/kg) or DHEC (15 mg/kg) + risperidone (10 mg/kg). $n = 6$ mice per group. Statistics: **c**, **e**, **g** Unpaired Student's t test for two-group comparison. **d**, **f**, **h**, **k**, **m** Log-rank test. **j**, **l** one-way ANOVA with Dunnett's multiple-comparison test. Source data are provided as a Source Data file.

---

previously[28,64]. Authentication of tumor models was performed with STR analysis and all GSCs were regularly tested negative for mycoplasma contamination. The available GSCs information are summarized in Supplementary Data 5.

The nonmalignant neural stem cell models ENSA and hNP1 were used in this study. ENSA (ENStem-A) is a human embryonic stem−derived neural progenitor cell obtained from Millipore Sigma

(Cat# SCC003). hNP1 (STEMEZ hNP1) is a human neural progenitor cell obtained from Neuromics (Cat# HN60001). 293 T cells obtained from ATCC (Cat# CRL-3216) were used to generate lentiviral particles. U937 cells obtained from ATCC(Cat# CRL-1593.2) were used to induced M1 macrophages. All these cells were authenticated by the supplier using STR analysis and were regularly tested negative for mycoplasma contamination.

In vivo tumorigenesis and animal experiments

All animal experiments were approved by the Institutional Animal Care and Use Committee (IACUC-2006033) at Nanjing Medical University in accordance with NIH and institutional guidelines. Both male and female mice were used in studies. BALB/c-Nude mice (Strain NO. D000521) and NCG mice (Strain NO. T001475) at 4 to 6 weeks of age were purchased from GemPharmatech (Nanjing, China). Mice were housed in a specific pathogen-free (SPF) facility under controlled conditions, including a 14-h light/10-h dark cycle, an ambient temperature of 22–24 °C, and relative humidity maintained at 40–60%. Pathogen-free environments were provided at the Animal Core Facility of Nanjing Medical University. Welfare monitoring, including supervision of housing conditions and animal status, was conducted daily by a veterinarian. Mice were monitored until neurologic signs were observed, at which point they were euthanised. Mice were euthanized using CO_2 inhalation followed by cervical dislocation to ensure death. All mice were randomly assigned to appropriate treatment groups. The investigators were blinded to the group allocation and study outcome assessments of all mice. The maximal tumor burden was strictly limited to 1.2 cm in diameter for mice, with a total tumor weight not exceeding 10% of the mice body weight. No animals exceeded these limits during the study. To monitor tumor growth in living animals, all GSCs used for the animal study were transduced with firefly luciferase through lentiviral infection.

For testing the in vivo inhibition effect of MEOX2 and SRGN knockdown. Inducible shMEOX2/shSRGN constructs (pTRIPZ) were purchased from Thermo Fisher Scientific. GSCs stably expressing firefly luciferase were infected with lentivirus carrying inducible pTRIPZ-shMEOX2 or pTRIPZ-shSRGN. 3028 (CL) or 2907 (MES) GSCs of shCONT, shMEOX2, or shSRGN cells (5×10^4) were then intracranially injected into the right frontal lobe at a depth of 3 mm. After GSCs implantation, the mice were observed daily and euthanized when they presented neurologic signs or became moribund. When the luciferase signals from tumor cells were detectable, mice were treated with the vehicle control or doxycycline (2 mg/ml in drinking water) to induce the expression of shMEOX2/shSRGN in xenografts. The size of the orthotopic tumor was monitored by the bioluminescence channel of the IVIS Spectrum.

For the WL1 xenograft model, we isolated EGFR-high (CL/AC-like cell-surface marker) and CD44-high (MES/MES-like cell-surface marker) cells from WL1. We then implanted these GSCs (1:1) orthotopically into immunocompromised mice to establish the model. For the subtype-mixed glioblastoma model. 1×10^4 3028 (CL) and 1×10^4 2907 (MES) GSCs were implanted into the right frontal lobe of mice. For the signaling pathway inhibitors, the concentrations in plasma and brain were determined by HPLC. When the luciferase signals from tumor cells were detectable, the drugs, water containing 2 mg/ml doxycycline or control water were administered. RG-4733 was administered orally by gavage, and PDTC was administered intraperitoneally. For the administration of four target inhibitors (Nilotinib, DHEC, Paliperidone, and Risperidone), after the establishment of the tumor-bearing mouse model, Nilotinib was administered orally by gavage, and the other three drugs were administered intraperitoneally. Finally, the size of the orthotopic tumor was monitored by the bioluminescence channel of the IVIS Spectrum.

Culture of glioblastoma stem cells and other cell models

GSCs were cultured as neurospheres in the neurobasal medium (Invitrogen) supplemented with 2% B27 supplement (Life Technologies), 1% L-glutamine, 1% sodium pyruvate, 20 ng/mL bFGF, and EGF (R&D Systems). GSCs were maintained and cultured as spheres for all experiments except immunofluorescence analyses, where cells were cultured as monolayers to facilitate imaging.

NSCs were cultured in neurobasal media supplemented with 2% B27, 20 ng/mL EGF, and bFGF. 293 T cells were cultured in DMEM with 10% fetal bovine serum (FBS). U937 cells were maintained in RPMI1640 medium containing 10% FBS.

Induction of glioblastoma stem cells to differentiated glioblastoma cells

For differentiation of GSCs to DGCs, fully grown neurospheres were collected and plated on normal cell culture dishes in Dulbecco's Modified Eagle Medium (DMEM) supplemented with 10% FBS and withdrawal of growth factors for 28 days.

Single-cell library preparation and sequencing

Cells from the samples in the scRNA-seq dataset collected from The First Affiliated Hospital of Nanjing Medical University were counted using a Countess instrument (ThermoFisher) and diluted to 700 to 1200 cells/µL. Cells were processed according to the Chromium single-cell RNA 3′ kit protocol (10X Genomics V2.0 chemistry) to capture 10,000 cells/chip positions. All the remaining procedures, including library construction, were performed according to the manufacturer's protocol. Libraries were quantified using an Agilent high-sensitivity DNA chip on a Bioanalyzer 2100 system (Agilent). Single-cell libraries were then sequenced on an Illumina HiSeqXTen instrument (PE150).

The cells collected from Beijing Tiantan Hospital were loaded into Chromium microfluidic chips with 3′ (10X Genomics V2.0) chemistry and barcoded with a 10X Chromium Controller (10X Genomics). RNA from the barcoded cells was subsequently reverse-transcribed, and sequencing libraries were constructed with a Chromium single-cell RNA 3′ v2 reagent kit (10X Genomics). The libraries were sequenced with an Illumina HiSeq 2000 (Illumina).

The single-cell sequencing data were analyzed using Cell Ranger (version 6.1.2, 10X Genomics) with default parameters. The data quality was assessed using the Seurat package (version 4.3.0).

Plasmids and lentiviral transduction

Lentiviral constructs expressing non-overlapping shRNAs directed against human MEOX2 (TRCN0000427218 and TRCN0000433531), human SRGN (TRCN0000007985 and TRCN0000007987), human NOTCH1 (TRCN0000003359 and TRCN0000350330), human NFKB1 (TRCN0000006517 and TRCN0000006520) or a non-targeting control shRNA (SHC002) with no targets in the human genome were obtained from Sigma-Aldrich. For CRISPR/Cas9 experiments, sgRNAs were cloned into the lentiCRISPR v2 plasmid (Addgene, Cat# 52961). All shRNAs and sgRNAs sequences are listed in Supplementary Data 8. Full-length human MEOX2, SRGN, NOTCH1, and NFKB1 in the pCMV6 vector were purchased from Origene and cloned into the BamHI and Xhol restriction sites of the pcDNA 3.1 vector (Invitrogen) for the overexpression assay. 293 T cells (ATCC, Cat# CRL-3216) were used to generate lentiviral particles by co-transfecting the packaging vectors psPAX2 and pMD2.G using a standard calcium phosphate transfection method in neurobasal complete medium.

Proliferation and neurosphere formation assays

Cell proliferation experiments were conducted by plating cells of interest at a density of 2000 cells/well in 96-well plates with six replicates. CellTiter-Glo (Promega, Cat# G7571) was used to measure cell viability on days 1, 3, 5, and 7. All data were normalized to day 1 and presented as mean ± SD. For the drug response test, 2000 cells were seeded under Notch signaling inhibitors (DAPT, RG-4733, Semagacestat), NF-κB signaling inhibitors (BAY11-7082, JSH-23, PDTC), drugs potential targeting MEOX2 (Nilotinib, DHEC, Imatinib, Abiraterone, Dutasteride, Lurasidone, etc.), and drugs potential targeting SRGN (Paliperidone, Risperidone, Conivaptan, Lumacaftor, Adapalene, Capmatinib, etc.) treatment. The plates were transferred to an incubator (37 °C, 5% CO_2) for 48 h. IC_{50} values of inhibitors and drugs were calculated with GraphPad Prism software.

Neurosphere formation was measured by in vitro limiting dilution. Briefly, decreasing numbers of cells per well (50, 20, 10, 5, and 1) were plated into 96-well plates. The presence and number of neurospheres in each well were recorded 14 days after plating. Extreme limiting dilution analysis was performed using software available at http://bioinf.wehi.edu.au/software/elda[65]. All proliferation and neurosphere experiments were performed with at least six replicates.

RNA isolation and quantitative RT-PCR
Total cellular RNA from cells was isolated by Trizol reagent (Takara, Cat# 9109). The PrimeScript cDNA Synthesis Kit (Takara, Cat# RR036A) was used for reverse transcription into cDNA. Quantitative real-time PCR was performed with an Applied Biosystems StepOnePlus cycler using SYBR-Green PCR Master Mix (ThermoFisher, Cat# A25742). All the primers used for qRT-PCR are listed in Supplementary Data 8.

Western blotting
For western blot analysis, cells and tissues were collected and lysed in RIPA buffer (50 mM Tris-HCl pH 7.5, 150 mM NaCl, 0.5% NP-40, 0.1% SDS and supplemented with protease inhibitors), then incubated on ice for 30 min. Lysates were centrifuged at 4 °C for 10 min at 12,000 rpm, and supernatants were collected. Supernatants were subjected to SDS-PAGE and transferred to polyvinylidene difluoride (PVDF) membranes (Millipore). The membranes were blocked with 5% non-fat milk for 2 h and then immunoblotted with primary antibodies overnight at 4 °C followed by the HRP-conjugated antibody at room temperature for 2 h. The blots were developed by SuperSignal West Pico PLUS Chemiluminescent Substrate (ThermoFisher, Cat# 34580). Antibodies used were as follows: anti-MEOX2 (Cat# DF3192, Affinity, 1:500), anti-SRGN (Cat#: PA5-51452, Invitrogen, 1:250), anti-SOX2 (Cat#: AF5140, Affinity, 1:500), anti-ID1 (Cat# DF2932, Affinity, 1:1000), anti-NFKB1 (Cat# 13586, Cell Signaling Technology, 1:1000), His-Tag antibody (Cat#: 12698, Cell Signaling Technology, 1:1000), Flag-Tag antibody (Cat# 14793, Cell Signaling Technology, 1:1000), HA-Tag antibody (Cat# 3724, Cell Signaling Technology, 1:1000), anti-beta Tubulin (Cat# AM1031a, Abcepta, 1:1000), anti-NOTCH1 (Cat# 3608, Cell Signaling Technology, 1:1000).

Immunofluorescence
Immunofluorescence experiments were performed using GBM surgical specimens or GSCs. Tumor samples from GBM patient surgical specimens were fixed in 4% paraformaldehyde at 4 °C, followed by cryoprotection with 30% sucrose in PBS at 4 °C. Paraffin section were stained with primary antibodies anti-SOX2 (R&D, AF2018, 1:100), anti-CD45 (abcam, ab40763, 1:100), anti-CD44 (Cat# 3570, Cell Signaling Technology, 1:200), anti-EGFR (Cat# 4267, Cell Signaling Technology, 1:50), anti-MEOX2 (Affinity, DF3152, 1:100) and anti-SRGN (Santa Cruz, sc-374657, 1:50). For GSCs, cells were fixed using 4% paraformaldehyde for 30 min and washed with PBS, permeabilized with 0.45% Triton X-100 for 10 min, and blocked in 3% bovine serum albumin (BSA) at room temperature for 2 h. Cells were incubated with appropriate primary antibodies anti-SRGN (Santa Cruz, Cat# sc-374657, 1:50), and anti-NFKB1 (Cell Signaling Technology, Cat# 13586, 1:200) at 4 °C overnight. The next day, the cells were washed 3 times with blocking buffer and incubated with secondary antibodies (Cell Signaling Technology, Cat #A4412 and Cat# A8890, 1:500). Images were captured with a Zeiss LSM700 microscope (Carl Zeiss) and processed using ImageJ software (NIH, Bethesda, MD, RRID:SCR_003070).

For Fig. 1i, j, Supplementary Fig. 1f, Supplementary Fig. 1g, Supplementary Fig. 3d, and Supplementary Fig. 3e, immunofluorescence images in each group were taken from the same section. The sections for Fig. 1i, j, Supplementary Fig. 1f and Supplementary Fig. 1g, and Supplementary Fig. 3d and Supplementary Fig. 3e were obtained from consecutive sections of the same sample.

Immunoprecipitation
GSCs transfected with the indicated constructs were collected and lysed in IP buffer (20 mM Tris-HCl, 150 mM NaCl 1% Triton X-100, 0.5% sodium deoxycholate, 1 mM DTT) containing PMSF and cocktail protease inhibitor at 4 °C for 30 mins, and followed by centrifugation at 14,000 g for 10 min at 4 °C. The lysates were incubated with IP antibody overnight at 4 °C. The supernatants were immunoprecipitated by incubation with Protein A/G Plus Agarose (ThermoFisher, Cat# 20423) at 4 °C for 2 h. Captured proteins were washed with IP buffer three times before immunoblotting and mass spectrometry analysis. Antibodies used were as follows: anti-SRGN (Cat# NBP1-80886, Novus, 1:100), anti-NFKB1 (Cat# 13586, Cell Signaling Technology, 1:100), Flag-Tag antibody (Cat# 14793, Cell Signaling Technology, 1:50).

Mass spectrometry
The identification of protein gel strips was to separate the sample proteins by gel electrophoresis, then obtain the protein gel strips at different positions on the film, and extract the peptides after enzymatic digestion. The peptides separated by liquid phase chromatography were ionized by a nanoESI source and then passed to a tandem mass spectrometer Q-Exactive HF X (Thermo Fisher Scientific, San Jose, CA) for DDA (Data Dependent Acquisition) mode detection. The protein identification uses experimental MS/MS data and aligns them with theoretical MS/MS data from the Uniprot protein database to obtain results. The main parameters were set: ion source voltage was set to 1.9 kV, MS1 scanning range was 350–1500 m/z; resolution was set to 60,000; MS2 starting m/z was fixed at 100; resolution was 15,000. The ion screening conditions for MS2 fragmentation: charge 2+ to 6 + , and the top 30 parent ions with the peak intensity exceeding 10,000. The ion fragmentation mode was HCD, and the fragment ions were detected in Orbitrap. The dynamic exclusion time was set to 30 s. The AGC was set to: MS1 3E6, MS2 1E5.

The whole process starts from converting raw MS data into a peak list and then searching matches in the UniProt protein database. Mascot (version 2.3.02) was used for protein identification. The mgf file was used as the original file. The parameters of Mascot are as follows: Enzyme: Trypsin. Peptide mass tolerance: 20 ppm. Fragment mass tolerance:0.05 Da. Fixed modifications: Carbamidomethyl (C). Variable modifications: Oxidation (M), Gln->pyro-Glu (N-term Q), Deamidated (NQ). Max missed cleavages: 1; Instrument type: ESI-FTICR. The output was then filtered by FDR 1% at spectral level (PSM-level FDR ≤ 0.01) to obtain a significant identified spectrum and peptide list. Finally, from the final protein identification list, analyses such as GO analysis (DAVID 6.8) were performed.

Flow cytometry and in vitro flow-based phagocytosis assay
U937-derived M1 macrophages were generated as macrophage model. Briefly, U937 cells were primed with PMA (Sigma, 5 nM) for 48 h to become unpolarized macrophages. To establish the M1 macrophages, the unpolarized macrophages were stimulated with 20 ng/ml of IFN-γ (Peprotech) and 100 ng/ml of LPS (Sigma) for an additional 48 h.

CL GSCs (3028) virally expressed Zsgreen and MES GSCs (2907) virally expressed mCherry. GSCs were transduced with shRNAs or pre-treated with drugs (two days). For all flow-based in vitro phagocytosis assays, GSCs (CL + MES, 1:1) and macrophages were co-cultured at a ratio of 2:1 in ultra-low-attachment 96-well U-bottom plates (Corning) in serum-free RPMI (Thermo Fisher Scientific). Co-cultured 3028-Zsgreen and 2907-mCherry were added to each well and co-incubated with the macrophages for 2 h at 37 °C. After co-culture, reactions were stained with anti-CD45 (BD Biosciences, Cat# 564879, 5 μl per test) to identify macrophages. Phagocytosis was evaluated as a sum of the Zsgreen+ or mCherry+ macrophages, expressed as a percentage of the total macrophages, as analyzed using FlowJo.

To isolate GSCs with distinct cellular states, cells were labeled with anti-CD44 (Cat# 559942, BD Biosciences, 20 μl per test) for MES-like,

anti-EGFR (Cat# 352903, Biolegend, 5 μl per test) for AC-like, anti-CD24 (Cat# 311121, Biolegend, 5 μl per test) for NPC-like, and anti-PDGFRA (Cat# 323507, Biolegend, 5 μl per test) for OPC-like states.

High-performance liquid chromatography (HPLC)

For six inhibitors, RG-4733 and DAPT were administered orally by gavage, and Semagacestat, BAY11-7082, JSH-23, and PDTC were administered intraperitoneally. Blood samples were collected from the faces of mice before and 0.5 h after drug administration. Serum was collected after $3000\,g$ centrifugation for 15 min. 50 μl serum was added to 150 μl methanol and vortex mixed for 10 min. The supernatant was centrifuged by $10,000\,g$ for 5 min. The corresponding mouse brain tissue was taken and weighed. After adding methanol with the same weight as the brain tissue, the Polytron HG-300 homogenizer was used to perform the homogenization. The homogenate was centrifuged at $10,000\,g$ for 10 min, 50 μl supernatant was taken, 150 μl methanol was added and the above operation was repeated. After measuring the standard curve for each drug according to the conditions recommended by the reagent manufacturer, the samples were measured and analyzed by High-Performance Liquid Chromatography (SHIMADZU).

Synergy assays

Cells were seeded in 96-well plates (2000 cells/well) and treated with the interval of concentration of drugs indicated for 48 h. Then, cell viability was assessed with CellTiter-Glo (Promega, Cat# G7571) assay and normalized to the untreated wells. Synergy was calculated using the HAS method using the SynergyFinder web application (https://synergyfinder.fimm.fi)[66].

Calculation of achievable Notch and NF-κB pathway inhibitors concentrations

Our studies used 200 mg/kg RG-4733 (Notch signaling inhibitor) after oral administration for 0.5 h, leading to a calculated brain concentration of $84.28 \pm 11.42\,\mu M$. We determined the concentration of the PDTC (NF-κB signaling inhibitor) after intraperitoneal injection of 100 mg/kg for 0.5 h. Using the same approach that we used for the RG-4733 concentration calculations, we estimated the brain concentration range of the PDTC as $88.92 \pm 3.04\,\mu M$. For animal experiments, we used 75 mg/kg RG-4733 and 50 mg/kg PDTC for each mouse. According to calculation, in vivo drug ranges for each agent achieved concentrations consistent with those we detected as having combinational benefit in IC50 concentrations from synergy assays.

Bio-Layer Interferometry (BLI)

Ni-NTA biosensors were loaded with His-tag recombinant human SRGN protein (Sino Biological Inc., Cat# LC15AU2001) and MEOX2 protein (Origene, Cat# AR51018PU-N) and then incubated with three compounds (Conivaptan, Cat# T6453; Risperidone, Cat# T0351; Paliperidone, Cat# T0076; Jervine, Cat# T3363; Targetmol) to generate an association curve (ForteBio Octet). The 60 s association phase was subsequently followed by a 90 s dissociation step to obtain the Kd value by the fitting curve.

Single-cell sequencing data processing and analysis

Single-cell sequencing data were processed to filter out low-quality reads with the following criteria: (1) 'N' bases accounting for ≥10% of the read length; (2) bases with quality <5 accounting for ≥50% of the read length; and (3) the reads contain adaptor sequence. The remaining reads were processed using the 10X cellranger pipeline (version 6.1.2) against the hg38 human reference genome to obtain the gene expression matrix. Gene-barcode count matrices were analyzed with the Seurat R package (version 4.3.0). Cells with <200 genes detected and >10% mitochondrial gene mapped reads were filtered from downstream analyses. Further, we removed the potential

doublets that occurred in the encapsulation step and/or as occasional pairs of cells that were not dissociated in sample preparation using the DoubletFinder package of the R.

After quality control, we normalized data by NormalizeData function in Seurat. The most variable 2000 genes were determined using the FindVariableGenes function with default parameters. We used the ScaleData function in Seurat to regress out UMI count and percentage of mitochondrial genes. PCA was performed using the RunPCA with these 2000 genes in Seurat.

We performed the 'RunHarmony' Harmony function to remove the effect of confounding factors in different samples. Dimensionality reduction was then performed using Harmony-adjusted space and UMAP plots were generated by the RunUMAP Seurat function. To identify cell clusters, we performed the FindNeighbors and FindClusters function in Seurat with the FindClusters parameter "resolution = 1".

To identify differentially expressed genes for each cell cluster, we used the FindMarkers function with default parameters in Seurat to evaluate the significance of each gene. These clusters were then labeled with particular cell states based on marker gene expression[7,8].

Tumor cells identification and GSC-like tumor cells prediction

CNAs were estimated by sorting the analyzed genes by their chromosomal location and applying a moving average to the relative expression values, with a sliding window of 100 genes within each chromosome[67]. Cells classified to each of the non-malignant cell types were used to define a baseline of normal karyotype. CNA analysis were performed using inferCNV. Cells were then classified as malignant by CNA analysis if they had high CNA signal. We then combined the CNA classification with the UMAP-based classifications, such that the final list of malignant cells included those which were classified as malignant by CNA, were part of the malignant UMAP cluster, and were not classified to any of the non-malignant cell types based on the marker gene-sets. We defined GSC-like tumor cells within malignant cells as any cells expressing CD133, CD15, or OCT4, in conjunction with SOX2.

Spatial transcriptomics analysis

The GBM spatial transcriptomic data used in this study are publicly available in the Datadryad database[27] [https://doi.org/10.5061/dryad.h70rxwdmj]. We analyzed 16 IDH-WT GBMs using SPATA2[27]. For spatial expression plots, we used scaled gene expression values (to plot single genes) or enrichment scores of a defined geneset. The x-axis and y-axis coordinates are given by the input file based on the localization to the H&E staining. The data are illustrated as surface plots (plotly package R-software).

Pan-cancer data collection and analysis

We analyzed MEOX2 and SRGN expression in all tumor types in TCGA. Uniformly processed TCGA RNA-seq (FPKM) data were obtained from the UCSC Xena server (https://xenabrowser.net/datapages/). Differential expression analysis was performed using R package limma.

Assignment of cells to metaprograms

For scRNA-seq and stRNA-seq data, cells were first annotated in the datasets (tumor cells, myeloid cells, oligodendrocytes, lymphocytes, endothelial cells, and fibroblasts). Tumor cells were assigned to the meta-module between the six meta-modules (MES1-like, MES2-like, NPC1-like, NPC2-like, AC-like, OPC-like) as previously described[8]. For most analyses, we collapsed the MES1 and MES2 groups of cells into one group of MES-like cells, and similarly, the NPC1 and NPC2 cells into one group of NPC-like cells. All signatures were subjected to a construction model using ssGSEA. To identify the exact molecular signatures in each cell analyzed by scRNA-seq, the signature score calculated by ssGSEA was evaluated using the permutation analysis[5]. One signature whose permutation p-value was smallest was taken as the main feature for the indicated cells.

For bulk RNA-seq data, the intrinsic subtypes (PN, CL, MES) of GSCs can be classified using ssGSEA on a 3 × 50 gene subset of the 7425 genes originally used for defining the subtypes with non-negative matrix factorization (NMF)[5].

RNA-seq and data analysis

DGCs were induced by their corresponding GSCs. For MEOX2 and SRGN knockout RNA-seq in CL GSC (3028) and MES GSC (2907), respectively. Patient-derived GSCs (3028 and 2907) were transduced with either control or two independent sgRNAs for MEOX2 (sgMEOX2-1 and sgMEOX2-2) or SRGN (sgSRGN-1 and sgSRGN-2), and successfully transduced cells were selected by puromycin for 3 days. Total RNA was extracted with Trizol reagent (Takara, Cat# 9109) according to the manufacturer's instructions. RNA sequencing was performed using MGI2000 platforms. FASTQ sequencing reads were trimmed using Trim Galore (https://github.com/FelixKrueger/TrimGalore), and transcript quantification was conducted using Salmon with the quasi-mapping mode. Salmon "quant" files were converted using Tximport, and differential expression analysis was performed using the R package limma. GSEA was performed by selecting differentially expressed genes, generating a pre-ranked list, and analyzing by R package clusterProfilter.

Chromatin immunoprecipitation (ChIP) assay and data analysis

4×10^6 cells per condition were collected, and ChIP assay was performed using the SimpleChIP Plus Enzymatic Chromatin IP Kit (Cell Signaling Technology, Cat# 9005) according to the manufacturer's protocols. Briefly, 10 μl MEOX2 antibody (Atlas, Cat# HPA053793, 1:50) or non-specific IgG was used for the immunoprecipitation of the DNA-protein immunocomplexes. Crosslinking was reversed by heating for 6 h at 65 °C, followed by digestion with proteinase K. In-depth whole-genome DNA sequencing was performed by BGI (Shenzhen, China). The data generated by Illumina sequencing passed quality control was compared with the human reference genome (hg38) sequence using Bowtie2, and finally peak detection and scanning were performed using MACS2. Input was used as a control for peak calling. ChIPseeker was used to annotate the peaks. Peaks and alignments were visualized using IGV.

Deconvolution analysis

Cellular proportions and cell state-specific gene expression matrices were inferred from bulk RNA-seq gene expression matrices using CIBERSORTx[68]. Reference scRNA-seq signature matrices were created from our internal 10x-derived scRNA-seq dataset using the 'Create Signature Matrix' module on the CIBERSORTx webserver (https://cibersortx.stanford.edu/) with default parameters and quantile normalization disabled. The CIBERSORTx webserver currently recommends users input no more than 5000 different single-cell profiles when creating their signature matrix. To meet this recommendation, our internal scRNA-seq dataset was randomly down sampled to 5000 cells using the 'sample' command in R with the seed set to 123. The cells not included in signature matrix formation were then set aside for validation analyses. For all runs, the bulk RNAseq dataset was input as the 'mixture' file and the respective signature matrix was input as the 'sigmatrix' file. For runs using our 10x-derived internal scRNAseq signatures, batch correction was done in 'S-mode' by setting the 'rmbatchSmode' parameter to TRUE.

Virtual screening

The Alphafold 2 database model was applied to predict the potential binding region of the target protein (Binding pocket of SRGN: 28-60 amino acids; DNA binding region of MEOX2: 187-246 amino acids), then proteins were docked with 2513 FDA-approved drugs via virtual screening. The score was ranked according to the value of Gibbs free energy (Supplementary Data 7).

Statistics and reproducibility

All data are shown as the mean ± SD. Statistical analyses were performed using GraphPad Prism with Student's t-test or ANOVA. For Kaplan–Meier survival curves, statistical differences between groups were determined by log-rank test. For all Fig. presented in a box-and-whisker format, the center line represents the median and the lower and upper limits of the box represent the 25th and 75th percentiles. The maximum and minimum are connected to the center box through the vertical lines. Blinding and randomization were performed in all experiments. This study complies with randomization in grouping age-matched mice into different experimental arms. The investigator was blinded to the group allocation during the experiment and/or when assessing the outcome. Sex and gender were not considered in the study design and analysis as it was not relevant to the research question being addressed.

Reporting summary

Further information on research design is available in the Nature Portfolio Reporting Summary linked to this article.

Data availability

The following publicly available datasets were used in this study. The GBM scRNA-seq are publicly available in the GEO database under accession code GSE103224[19]. The GBM scRNA-seq are publicly available in the GEO database under accession code GSE141383[21]. The GBM scRNA-seq are publicly available in the GEO database under accession code GSE173278[22]. The GBM scRNA-seq are publicly available in the GEO database under accession code GSE182109[23]. The GBM scRNA-seq are publicly available in the GEO database under accession code GSE117891[20]. The GBM scRNA-seq are publicly available in the GEO database under accession code GSE131928[8]. The GBM spatial transcriptomic data are publicly available in the Datadryad database[27] [https://doi.org/10.5061/dryad.h70rxwdmj]. The GSCs/NSCs bulk RNA-seq data are available in the GEO database under accession code GSE119834[28]. The GSCs/NSCs H3K27ac ChIP-seq data are available in the GEO database under accession code GSE119775[28]. The TCGA GBM datasets (Affymetrix U133a microarray) were obtained from the UCSC website (https://xenabrowser.net). CGGA, Rembrandt, and Ivy GAP datasets were downloaded from GlioVis[69] (http://gliovis.bioinfo.cnio.es/). All raw data from the newly generated datasets have been deposited. The following datasets were generated in this study. The GBM scRNA-seq data have been deposited in the GSA database under accession code HRA004899. The HRA004899 dataset is available under controlled access in compliance with China's Regulations on the Management of Human Genetic Resources (State Council Order No. 717, 2019) and the Biosecurity Law of the People's Republic of China (2021), which govern the management and sharing of Chinese genomic data in GSA[70]. Access can be obtained by contacting Dr. Xiuxing Wang. Access will be granted to researchers affiliated with academic or research institutions for non-commercial purposes, following review and approval of a formal data access request. Requests for data access will be responded to within 7 days. Once access is granted, the data will remain available to the approved user for a period of 1 year. The GSCs scRNA-seq data have been deposited in the GSA database under accession code HRA010016. The GSCs/DGCs bulk RNA-seq data have been deposited in the GSA database under accession code HRA006647. The GSC3028 bulk RNA-seq and ChIP-seq data have been deposited in the GSA database under accession code HRA004902. The GSC2907 bulk RNA-seq have been deposited in the GSA database under accession code HRA004930. The GSC2907 SRGN IP mass spectrometry data are deposited in the PRIDE database under accession code PXD061009. The HRA010016, HRA006647, HRA004902, and HRA004930 datasets are open access. Source data are provided with this paper. The remaining data are available within

the Article, Supplementary Information or Source Data file. Source data are provided with this paper.

References

1. McKinnon, C., Nandhabalan, M., Murray, S. A. & Plaha, P. Glioblastoma: clinical presentation, diagnosis, and management. *BMJ* **374**, n1560 (2021).
2. Cantrell, J. N. et al. Progress toward long-term survivors of glioblastoma. *Mayo Clin. Proc.* **94**, 1278–1286 (2019).
3. Yabo, Y. A., Niclou, S. P. & Golebiewska, A. Cancer cell heterogeneity and plasticity: a paradigm shift in glioblastoma. *Neuro Oncol.* **24**, 669–682 (2022).
4. Tan, A. C. et al. Management of glioblastoma: State of the art and future directions. *CA Cancer J. Clin.* **70**, 299–312 (2020).
5. Wang, Q. et al. Tumor evolution of glioma-intrinsic gene expression subtypes associates with immunological changes in the microenvironment. *Cancer Cell* **32**, 42–56.e46 (2017).
6. Verhaak, R. G. et al. Integrated genomic analysis identifies clinically relevant subtypes of glioblastoma characterized by abnormalities in PDGFRA, IDH1, EGFR, and NF1. *Cancer Cell* **17**, 98–110 (2010).
7. Johnson, K. C. et al. Single-cell multimodal glioma analyses identify epigenetic regulators of cellular plasticity and environmental stress response. *Nat. Genet.* **53**, 1456–1468 (2021).
8. Neftel, C. et al. An integrative model of cellular states, plasticity, and genetics for glioblastoma. *Cell* **178**, 835–849.e821 (2019).
9. Venteicher, A. S. et al. Decoupling genetics, lineages, and microenvironment in IDH-mutant gliomas by single-cell RNA-seq. *Science* **355**, eaai8478 (2017).
10. Patel, A. P. et al. Single-cell RNA-seq highlights intratumoral heterogeneity in primary glioblastoma. *Science* **344**, 1396–1401 (2014).
11. Bao, S. et al. Glioma stem cells promote radioresistance by preferential activation of the DNA damage response. *Nature* **444**, 756–760 (2006).
12. Chen, J. et al. A restricted cell population propagates glioblastoma growth after chemotherapy. *Nature* **488**, 522–526 (2012).
13. Cheng, L. et al. Glioblastoma stem cells generate vascular pericytes to support vessel function and tumor growth. *Cell* **153**, 139–152 (2013).
14. Rusu, P. et al. GPD1 specifically marks dormant glioma stem cells with a distinct metabolic profile. *Cell Stem Cell* **25**, 241–257.e248 (2019).
15. Osswald, M. et al. Brain tumour cells interconnect to a functional and resistant network. *Nature* **528**, 93–98 (2015).
16. Kim, D. et al. SHMT2 drives glioma cell survival in ischaemia but imposes a dependence on glycine clearance. *Nature* **520**, 363–367 (2015).
17. Suva, M. L. & Tirosh, I. The glioma stem cell model in the era of single-cell genomics. *Cancer Cell* **37**, 630–636 (2020).
18. Jin, X. et al. Targeting glioma stem cells through combined BMI1 and EZH2 inhibition. *Nat. Med.* **23**, 1352–1361 (2017).
19. Yuan, J. et al. Single-cell transcriptome analysis of lineage diversity in high-grade glioma. *Genome Med.* **10**, 57 (2018).
20. Yu, K. et al. Surveying brain tumor heterogeneity by single-cell RNA-sequencing of multi-sector biopsies. *Natl Sci. Rev.* **7**, 1306–1318 (2020).
21. Chen, A. X. et al. Single-cell characterization of macrophages in glioblastoma reveals MARCO as a mesenchymal pro-tumor marker. *Genome Med.* **13**, 88 (2021).
22. LeBlanc, V. G. et al. Single-cell landscapes of primary glioblastomas and matched explants and cell lines show variable retention of inter- and intratumor heterogeneity. *Cancer Cell* **40**, 379–392.e379 (2022).
23. Abdelfattah, N. et al. Single-cell analysis of human glioma and immune cells identifies S100A4 as an immunotherapy target. *Nat. Commun.* **13**, 767 (2022).
24. Bhaduri, A. et al. Outer radial glia-like cancer stem cells contribute to heterogeneity of glioblastoma. *Cell Stem Cell* **26**, 48–63.e46 (2020).
25. Zhou, W. et al. Periostin secreted by glioblastoma stem cells recruits M2 tumour-associated macrophages and promotes malignant growth. *Nat. Cell Biol.* **17**, 170–182 (2015).
26. Pyonteck, S. M. et al. CSF-1R inhibition alters macrophage polarization and blocks glioma progression. *Nat. Med.* **19**, 1264–1272 (2013).
27. Ravi, V. M. et al. Spatially resolved multi-omics deciphers bidirectional tumor-host interdependence in glioblastoma. *Cancer Cell* **40**, 639–655.e613 (2022).
28. Mack, S. C. et al. Chromatin landscapes reveal developmentally encoded transcriptional states that define human glioblastoma. *J. Exp. Med.* **216**, 1071–1090 (2019).
29. Zhao, Z. & Shilatifard, A. Epigenetic modifications of histones in cancer. *Genome Biol.* **20**, 245 (2019).
30. Yang, Y. et al. ECSIT facilitates memory CD8(+) T cell development by mediating fumarate synthesis during viral infection and tumorigenesis. *Nat. Cell Biol.* **26**, 450–463 (2024).
31. Avila-Moreno, F. et al. Overexpression of MEOX2 and TWIST1 is associated with H3K27me3 levels and determines lung cancer chemoresistance and prognosis. *PLoS ONE* **9**, e114104 (2014).
32. Garcia-Fernandez, J. The genesis and evolution of homeobox gene clusters. *Nat. Rev. Genet.* **6**, 881–892 (2005).
33. Mankoo, B. S. et al. Mox2 is a component of the genetic hierarchy controlling limb muscle development. *Nature* **400**, 69–73 (1999).
34. Newman, A. M. et al. Determining cell type abundance and expression from bulk tissues with digital cytometry. *Nat. Biotechnol.* **37**, 773–782 (2019).
35. Bindea, G. et al. Spatiotemporal dynamics of intratumoral immune cells reveal the immune landscape in human cancer. *Immunity* **39**, 782–795 (2013).
36. Jumper, J. et al. Highly accurate protein structure prediction with AlphaFold. *Nature* **596**, 583–589 (2021).
37. Wang, F. et al. ABL1, overexpressed in hepatocellular carcinomas, regulates expression of NOTCH1 and promotes development of liver tumors in mice. *Gastroenterology* **159**, 289–305.e216 (2020).
38. Lei, X. et al. The FDA-approved natural product dihydroergocristine reduces the production of the Alzheimer's disease amyloid-beta peptides. *Sci. Rep.* **5**, 16541 (2015).
39. Rehman, S. et al. Unraveling enhanced brain delivery of paliperidone-loaded lipid nanoconstructs: pharmacokinetic, behavioral, biochemical, and histological aspects. *Drug. Deliv.* **29**, 1409–1422 (2022).
40. Yousefi-Manesh, H. et al. Risperidone attenuates acetic acid-induced colitis in rats through inhibition of TLR4/NF-kB signaling pathway. *Immunopharmacol. Immunotoxicol.* **42**, 464–472 (2020).
41. Louis, D. N. et al. The 2016 World Health Organization Classification of tumors of the central nervous system: a summary. *Acta Neuropathol.* **131**, 803–820 (2016).
42. Barthel, F. P. et al. Longitudinal molecular trajectories of diffuse glioma in adults. *Nature* **576**, 112–120 (2019).
43. Klughammer, J. et al. The DNA methylation landscape of glioblastoma disease progression shows extensive heterogeneity in time and space. *Nat. Med.* **24**, 1611–1624 (2018).
44. Korber, V. et al. Evolutionary Trajectories of IDH(WT) glioblastomas reveal a common path of early tumorigenesis instigated years ahead of initial diagnosis. *Cancer Cell* **35**, 692–704.e612 (2019).
45. Mazor, T. et al. DNA methylation and somatic mutations converge on the cell cycle and define similar evolutionary histories in brain tumors. *Cancer Cell* **28**, 307–317 (2015).
46. Flavahan, W. A., Gaskell, E. & Bernstein, B. E. Epigenetic plasticity and the hallmarks of cancer. *Science* **357**, eaal2380 (2017).
47. Liau, B. B. et al. Adaptive chromatin remodeling drives glioblastoma stem cell plasticity and drug tolerance. *Cell Stem Cell* **20**, 233–246.e237 (2017).
48. Kim, Y. et al. Perspective of mesenchymal transformation in glioblastoma. *Acta Neuropathol. Commun.* **9**, 50 (2021).

49. Chaligne, R. et al. Epigenetic encoding, heritability and plasticity of glioma transcriptional cell states. *Nat. Genet.* **53**, 1469–1479 (2021).

50. Wang, R. et al. Glioblastoma stem-like cells give rise to tumour endothelium. *Nature* **468**, 829–833 (2010).

51. Kachgal, S., Mace, K. A. & Boudreau, N. J. The dual roles of homeobox genes in vascularization and wound healing. *Cell Adh. Migr.* **6**, 457–470 (2012).

52. Wang, J. et al. MEOX2-mediated regulation of Cathepsin S promotes cell proliferation and motility in glioma. *Cell Death Dis.* **13**, 360 (2022).

53. Tachon, G. et al. MEOX2 transcription factor is involved in survival and adhesion of glioma stem-like cells. *Cancers* **13**, 5943 (2021).

54. Manou, D., Karamanos, N. K. & Theocharis, A. D. Tumorigenic functions of serglycin: regulatory roles in epithelial to mesenchymal transition and oncogenic signaling. *Semin. Cancer Biol.* **62**, 108–115 (2020).

55. Manou, D. et al. The expression of serglycin is required for active transforming growth factor beta receptor i tumorigenic signaling in glioblastoma cells and paracrine activation of stromal fibroblasts via CXCR-2. *Biomolecules* **14**, 461 (2024).

56. Roy, A. et al. Serglycin as a potential biomarker for glioma: association of serglycin expression, extent of mast cell recruitment and glioblastoma progression. *Oncotarget* **8**, 24815–24827 (2017).

57. Chao, M. P. et al. Calreticulin is the dominant pro-phagocytic signal on multiple human cancers and is counterbalanced by CD47. *Sci. Transl. Med.* **2**, 63ra94 (2010).

58. Feng, M. et al. Phagocytosis checkpoints as new targets for cancer immunotherapy. *Nat. Rev. Cancer* **19**, 568–586 (2019).

59. Zhai, K. et al. Pharmacological inhibition of BACE1 suppresses glioblastoma growth by stimulating macrophage phagocytosis of tumor cells. *Nat. Cancer* **2**, 1136–1151 (2021).

60. Hutter, G. et al. Microglia are effector cells of CD47-SIRPalpha antiphagocytic axis disruption against glioblastoma. *Proc. Natl. Acad. Sci. USA* **116**, 997–1006 (2019).

61. Gholamin, S. et al. Disrupting the CD47-SIRPalpha anti-phagocytic axis by a humanized anti-CD47 antibody is an efficacious treatment for malignant pediatric brain tumors. *Sci. Transl. Med.* **9**, eaaf2968 (2017).

62. Friedman, H. S. et al. Bevacizumab alone and in combination with irinotecan in recurrent glioblastoma. *J. Clin. Oncol.* **27**, 4733–4740 (2009).

63. Nicholson, J. G. & Fine, H. A. Diffuse glioma heterogeneity and its therapeutic implications. *Cancer Discov.* **11**, 575–590 (2021).

64. Yuan, H. et al. Lysine catabolism reprograms tumour immunity through histone crotonylation. *Nature* **617**, 818–826 (2023).

65. Hu, Y. & Smyth, G. K. ELDA: extreme limiting dilution analysis for comparing depleted and enriched populations in stem cell and other assays. *J. Immunol. Methods* **347**, 70–78 (2009).

66. Ianevski, A., Giri, A. K. & Aittokallio, T. SynergyFinder 3.0: an interactive analysis and consensus interpretation of multi-drug synergies across multiple samples. *Nucleic Acids Res.* **50**, W739–W743 (2022).

67. Tirosh, I. et al. Single-cell RNA-seq supports a developmental hierarchy in human oligodendroglioma. *Nature* **539**, 309–313 (2016).

68. Goldman, M. J. et al. Visualizing and interpreting cancer genomics data via the Xena platform. *Nat. Biotechnol.* **38**, 675–678 (2020).

69. Bowman, R. L., Wang, Q., Carro, A., Verhaak, R. G. & Squatrito, M. GlioVis data portal for visualization and analysis of brain tumor expression datasets. *Neuro Oncol.* **19**, 139–141 (2017).

70. Members, C.-N. Partners. Database resources of the national genomics data center, china national center for bioinformation in 2022. *Nucleic Acids Res.* **50**, D27–D38 (2022).

Author contributions

Conceptualization, Y.Y., J.N.R., W.Z., and X.W.; Methodology, CF.L. and T.K.; Bioinformatics Analysis, CF.L. and Q.L.; Validation, CF.L., T.K., Y.L., and K.S.; Formal Analysis, CF.L., T.K, J.Z, and K.Y.; Investigation, CF.L., T.K., and X.F.; Resources, J.Z., W.Z., J.N.R., Y.Y., and X.W.; Data Curation, CF.L., T.K., D.L., D.S., J.G., D.G., HA.Y., YQ.L., J.Y., and X.W.; Project Administration, Q.Z., Z.S., and QL.W.; Technical Support, L.Z., Z.Q., HU.Y., NW.Z., W.G., W.T., YM.L, Y.C., J.J., C.K., J.M., S.A., QH.W., F.L., X.Q., S.C.M, Z.H., CJ.L., M.D.T, N.Z., and M.L.; Funding Acquisition, N.L., Y.Y., and X.W.; Writing – Original Draft, CF.L., K.Y., Z.Z., D.D., and R.C.G; Writing – Review & Editing, All authors; Supervision, Y.Y., J.N.R., W.Z., and X.W.

Competing interests

The authors declare no competing interests.

Additional information

Supplementary information The online version contains supplementary material available at https://doi.org/10.1038/s41467-025-58366-5.

Correspondence and requests for materials should be addressed to Yongping You, Jeremy N. Rich, Wei Zhang or Xiuxing Wang.

Peer review information *Nature Communications* thanks the anonymous reviewers for their contribution to the peer review of this work. A peer review file is available.

Reprints and permissions information is available at http://www.nature.com/reprints

Publisher's note Springer Nature remains neutral with regard to jurisdictional claims in published maps and institutional affiliations.

Chenfei Lu[1,2,3,19], Tao Kang[2,3,19], Junxia Zhang[1,19], Kailin Yang[4,19], Yang Liu[5,19], Kefan Song[1], Qiankun Lin[2,3], Deobrat Dixit[6], Ryan C. Gimple[4], Qian Zhang[2,3], Zhumei Shi[1], Xiao Fan[1], Qiulian Wu[6], Daqi Li[2,3], Danyang Shan[2,3], Jiancheng Gao[1,2,3], Danling Gu[2,3], Hao You[2,3], Yangqing Li[2,3], Junlei Yang[2,3], Linjie Zhao[6], Zhixin Qiu[7], Hui Yang[8], Ningwei Zhao[9], Wei Gao[2], Weiwei Tao[10], Yingmei Lu[2], Yun Chen[2], Jing Ji[1], Zhe Zhu[11], Chunsheng Kang[12], Jianghong Man[13], Sameer Agnihotri[6], Qianghu Wang[3], Fan Lin[2], Xu Qian[3], Stephen C. Mack[14], Zhibin Hu[3], Chaojun Li[3], Michael D. Taylor[15], Ning Liu[1], Nu Zhang[16], Ming Lu[2], Yongping You[1,3]✉, Jeremy N. Rich[6]✉, Wei Zhang[17]✉ & Xiuxing Wang[1,2,3,18]✉

¹Department of Neurosurgery, The First Affiliated Hospital of Nanjing Medical University, Nanjing, Jiangsu, China. ²Department of Cell Biology, National Health Commission Key Laboratory of Antibody Techniques, Jiangsu Provincial Key Laboratory of Human Functional Genomics, School of Basic Medical Sciences, Nanjing Medical University, Nanjing, Jiangsu, China. ³Institute for Brain Tumors, Jiangsu Key Lab of Cancer Biomarkers, Prevention and Treatment, Collaborative Innovation Center for Cancer Personalized Medicine, Nanjing Medical University, Nanjing, Jiangsu, China. ⁴Department of Radiation Oncology, Taussig Cancer Center, Cleveland Clinic, Cleveland, OH, USA. ⁵Department of Pharmacology, School of Medicine and Holistic Integrative Medicine, Nanjing University of Chinese Medicine, Nanjing, Jiangsu, China. ⁶University of Pittsburgh Medical Center Hillman Cancer Center, Pittsburgh, PA, USA. ⁷Department of Anesthesiology, Zhongshan Hospital, Institute for Translational Brain Research, State Key Laboratory of Medical Neurobiology, MOE Frontiers Center for Brain Science, Fudan University, Shanghai, China. ⁸Department of Neurosurgery, Huashan Hospital, Fudan University, Shanghai, China. ⁹Affiliated Hospital of Nanjing University of Chinese Medicine, Nanjing, China. ¹⁰College of Biomedicine and Health & College of Life Science and Technology, Huazhong Agricultural University, Wuhan, Hubei, China. ¹¹Department of Pathology and Cell Biology, Columbia University Irving Medical Center, New York, NY, USA. ¹²Laboratory of Neuro-oncology, Tianjin Neurological Institute, Tianjin Medical University General Hospital, Tianjin, China. ¹³State Key Laboratory of Proteomics, National Center of Biomedical Analysis, Beijing, China. ¹⁴Department of Developmental Neurobiology, Neurobiology and Brain Tumor Program, St. Jude Children's Research Hospital, Memphis, TN, USA. ¹⁵Department of Pediatrics- Hematology/Oncology and Neurosurgery, Texas Children's Cancer Center, Hematology-Oncology Section, Baylor College of Medicine, Houston, Texas, USA. ¹⁶Department of Neurosurgery, The First Affiliated Hospital of Sun Yat-sen University, Guangzhou, Guangdong, China. ¹⁷Department of Neurosurgery, Beijing Tiantan Hospital, Capital Medical University, Beijing, China. ¹⁸Jiangsu Cancer Hospital, Affiliated Cancer Hospital of Nanjing Medical University, Nanjing, Jiangsu, China. ¹⁹These authors contributed equally: Chenfei Lu, Tao Kang, Junxia Zhang, Kailin Yang, Yang Liu. ✉e-mail: yypl9@njmu.edu.cn; drjeremyrich@gmail.com; zhangwei_vincent@126.com; drxiuxingwang@163.com